

American University in Cairo

AUC Knowledge Fountain

Archived Theses and Dissertations

6-1-2008

Analysis of the flow through a Francis' turbine runner using computational fluid dynamics

William Anthony

Follow this and additional works at: https://fount.aucegypt.edu/retro_etds

Recommended Citation

APA Citation

Anthony, W. (2008). *Analysis of the flow through a Francis' turbine runner using computational fluid dynamics* [Master's thesis, the American University in Cairo]. AUC Knowledge Fountain.

https://fount.aucegypt.edu/retro_etds/2313

MLA Citation

Anthony, William. *Analysis of the flow through a Francis' turbine runner using computational fluid dynamics*. 2008. American University in Cairo, Master's thesis. *AUC Knowledge Fountain*.

https://fount.aucegypt.edu/retro_etds/2313

This Thesis is brought to you for free and open access by AUC Knowledge Fountain. It has been accepted for inclusion in Archived Theses and Dissertations by an authorized administrator of AUC Knowledge Fountain. For more information, please contact mark.muehlhaeusler@aucegypt.edu.

The American University in Cairo

School of Sciences and Engineering

ANALYSIS OF THE FLOW THROUGH A FRANCIS TURBINE RUNNER USING
COMPUTATIONAL FLUID DYNAMICS

A Thesis Submitted to

Interdisciplinary Engineering Department

in partial fulfillment of the requirements for the degree of Master of Science

By

William Anthony

BSc.(Mechanical Engineering)

Under the supervision of

Dr. Amr Serag El Din, Dr. Ashraf Sabry and Dr. Lamyaa El-Gabry

February, 2008

The American University in Cairo

ANALYSIS OF THE FLOW THROUGH A FRANCIS TURBINE RUNNER USING
COMPUTATIONAL FLUID DYNAMICS

A Thesis Submitted by William Anthony
To Department of Interdisciplinary Engineering

December 2007

In partial fulfillment of the requirements for

The degree of Master of Science

Has been approved by

Dr.
Thesis Committee Chair/Advisor
Affiliation

Dr.
Thesis Committee Reader/ Examiner
Affiliation

Dr.
Thesis Committee Reader/Examiner
Affiliation

Department Chair/
Program Director

Date

Dean

Date

DEDICATION

This study is dedicated to Maj. Gen. (rtd.) Henry K. Anyidoho for his encouragement and support in ensuring the fulfillment of my aspiration

ACKNOWLEDGMENT

I acknowledge the diverse support of Ms. Sawsan Mardini and the African Graduate Fellowship, the Engineering Department, Writing Center, Mrs. Akweley Plahar-Aryee and the Staff of the Ghana Embassy in Egypt, Mr. M.N Sackey, Francis Akwensivie, Ms. Frankke Ortega, Ms. Edith Hammett, Ms. Cynthia J. Bolanos, Mr. Timothy Anyidoho, Mr. Ernest Abbey, Mr. Daniel Odoi, Lt. Ebenezer Laryea Odumang and Ms. Rita Ablordeppey in ensuring my successful return and completion of my study. I wish to also acknowledge the support of Eng. Reda for providing the DesignFOIL software used in obtaining the blade profile, and his assistance in the use of it and FLUENT; as well as, to thank Eng. M. Sawy for making the CAD Lab available during the period of study.

Kudos, and may the good Lord bless you all.

American University in Cairo

Analysis of the Flow through a Francis' Turbine Runner Using Computational Fluid
Dynamics

William Anthony

Dr. Amr Serag El Din, Dr. Ashraf Sabry and Dr. Lamyaa El-Gabry

ABSTRACT

This study investigates the fluid flow through the runner of an exceptionally low specific speed Francis' turbine using computational fluid dynamics (CFD) to predict some performance characteristic of the runner, and to determine the effect of cavitation on the flow features within the turbine. It employs FLUENT CFD codes for the analysis. The study was carried out under steady conditions in two- dimensional analysis, primarily using the RNG k- ϵ turbulence model. It is mainly on single phase analysis; however a single case of two-phase cavitation modeling was performed in order to evaluate cavitation effects.

The hydraulic losses were much dependent on the inlet flow velocity and less dependent on the rotational speed. Cavitation occurred throughout the flow domain and this led to non-physical negative pressure predictions for the single phase analysis. For a fixed discharge, cavitation had significant effect on the prediction of the torque and hence the runner

efficiency obtained from the CFD analysis. It causes a significant reduction of the runner efficiency by increasing the hydraulic losses and should be considered in the analysis of the flow features within a runner which is likely to experience cavitation in order to overcome some of the shortcomings of the single phase predictions.

TABLE OF CONTENTS

Approval Page	ii
Dedication	iii
Acknowledgement	iv
Abstract	v
List of Tables.....	x
List of Figures.....	xii
CHAPTER ONE: INTRODUCTION.....	1
1.0 Background Introduction	1
1.1 Objectives of the Study.....	2
1.2 Methodology.....	2
1.3 Scope of the Study	2
CHAPTER TWO: LITERATURE REVIEW.....	3
2.0 General Introduction	3
2.1 Radial Hydraulic Turbine	3
2.2 Computational Fluid Dynamics	4
2.3 Numerical Investigation and Validation of Flow in Hydraulic Turbines	7
2.4 Challenges and the Future of CFD Analysis of Hydraulic Turbines	12
2.5 Some Successful Applications of CFD Analysis.....	13

CHAPTER THREE: MODELING.....	15
3.0 Introduction to FLUENT	15
3.1 k- ϵ Turbulence Model.....	16
3.2 CFD Modeling of the Francis' Turbine Runner	17
3.2.1 Boundary Conditions	17
3.2.2 Specification of Turbulence Parameters	21
3.3 Specification of the Francis' Turbine Runner	22
3.3.1 Blade	22
3.4 Meshing, Solver and the Convergence Criteria	23
3.4.1 Meshing	23
3.4.2 The Solver and Turbulence Model	25
3.4.3 Convergence Criteria	26
CHAPTER FOUR: SINGLE PHASE BLADE TO BLADE FLOW ANALYSIS.....	27
4.0 Results and Discussion for the Single Phase Analysis.....	27
CHAPTER FIVE: CAVITATION MODELING AND ANALYSIS.....	74
5.0 Introduction.....	74
5.1 Modeling Cavitation	74
5.2 Results and Comparative Analysis	75
CHAPTER SIX: SUMMARY CONCLUSION, LIMITATION AND FUTURE EXTENSION.....	84
6.0 Summary Conclusion	84

6.1 Limitation of the Study.....	85
6.2 Future Extension	85
REFERENCES	87

LIST OF TABLES

Table 1	CFD Predictions of Flow Properties at 173.1 rpm Rotational Speed and at 20 m/s Velocity Inlet
Table 2	CFD Predictions of Flow Properties at 173.1 rpm Rotational Speed and at 25 m/s Velocity Inlet
Table 3	CFD Predictions of Flow Properties at 173.1 rpm Rotational Speed and at 30 m/s Velocity Inlet
Table 4	CFD Predictions of Flow Properties at 173.1 rpm Rotational Speed and at 35m/s Velocity Inlet
Table 5	CFD Predictions of Flow Properties at 173.1 rpm Rotational Speed and at 40 m/s Velocity Inlet
Table 6	CFD Predictions of Flow Properties at 115.4 rpm Rotational Speed and at 20 m/s Velocity Inlet
Table 7	CFD Predictions of Flow Properties at 115.4 rpm Rotational Speed and at 25 m/s Velocity Inlet
Table 8	CFD Predictions of Flow Properties at 115.4 rpm Rotational Speed and at 30 m/s Velocity Inlet
Table 9	CFD Predictions of Flow Properties at 115.4 rpm Rotational Speed and at 35 m/s Velocity Inlet
Table 10	CFD Predictions of Flow Properties at 115.4 rpm Rotational Speed and at 40 m/s Velocity Inlet
Table 11	CFD Predictions of Flow Properties at 76.9 rpm Rotational Speed and at 20 m/s Velocity Inlet
Table 12	CFD Predictions of Flow Properties at 76.9 rpm Rotational Speed and at 25 m/s Velocity Inlet
Table 13	CFD Predictions of Flow Properties at 76.9 rpm Rotational Speed and at 30 m/s Velocity Inlet
Table 14	CFD Predictions of Flow Properties at 76.9 rpm Rotational Speed and at 35 m/s Velocity Inlet
Table 15	CFD Predictions of Flow Properties at 76.9 rpm Rotational Speed and at 40 m/s Velocity Inlet

Table 16 Effect of Cavitation on the Flow Properties

LIST OF FIGURES

- Figure 3.1 Display of the Model and the Allocation of Boundary Conditions
- Figure 3.2 Grid Display of the Model after Adaptation
- Figure 3.3 Grid Display of the Periodic Model
- Figure 4.1 Convergence History for the case with Inlet Velocity of 25 m/s and Inlet Flow Angle of 45 degree
- Figure 4.2 Contour Plot of Static Pressure Distribution for the Case with Inlet Velocity of 25 m/s and Inlet Flow Angle of 45 degree
- Figure 4.3 Absolute Velocity Vector Plot for the Case with Inlet Velocity of 25 m/s and Inlet Flow Angle of 45 degree
- Figure 4.4 Relative Velocity Vector Plot for the Case with Inlet Velocity of 25 m/s and Inlet Flow Angle of 45 degree
- Figure 4.5 Contour Plot of Total Pressure Distribution for the Case with Inlet Velocity of 25 m/s and Inlet Flow Angle of 45 degree
- Figure 4.6 Convergence History for the case with Inlet Velocity of 40 m/s and Inlet Flow Angle of 60 degree
- Figure 4.7 Contour Plot of Static Pressure Distribution for the Case with Inlet Velocity of 40 m/s and Inlet Flow Angle of 60 degree
- Figure 4.8 Absolute Velocity Vector Plot for the Case with Inlet Velocity of 40 m/s and Inlet Flow Angle of 60 degree
- Figure 4.9 Relative Velocity Vector Plot for the Case with Inlet Velocity of 40 m/s and Inlet Flow Angle of 60 degree
- Figure 4.10 Plot of Inlet Flow Angle against Neutralized Discharge
- Figure 4.11 Plot of Inlet Flow Angle against Neutralized Hydraulic Losses
- Figure 4.12 Plot of Inlet Flow Angle against Neutralized Net Head
- Figure 4.13 Plot of Inlet Flow Angle against Neutralized Power Output
- Figure 4.14 Plot of Inlet Flow Angle against Runner Efficiency

- Figure 4.15 Plot of Inlet Flow Angle against Neutralized Discharge at Varying Rotational Speed
- Figure 4.16 Plot of Inlet Flow Angle against Neutralized Net Head at Varying Rotational Speed
- Figure 4.17 Plot of Inlet Flow Angle against Neutralized Flow Losses at Varying Rotational Speed
- Figure 4.18 Plot of Inlet Flow Angle against Neutralized Power Output at Varying Rotational Speed
- Figure 4.19 Plot of Inlet Flow Angle against Runner Efficiency at Varying Rotational Speed
- Figure 5.1 Convergence History for the case with Inlet Velocity of 40 m/s and Inlet Flow Angle of 60 degree (with Cavitation)
- Figure 5.2 Contour Plot of Static Absolute Pressure Distribution for the Case with Inlet Velocity of 40 m/s and Inlet Flow Angle of 60 degree (with Cavitation)
- Figure 5.3 Absolute Velocity Vector Plot for the Case with Inlet Velocity of 40 m/s and Inlet Flow Angle of 60 degree (with Cavitation)
- Figure 5.4 Relative Velocity Vector Plot for the Case with Inlet Velocity of 40 m/s and Inlet Flow Angle of 60 degree (with Cavitation)
- Figure 5.5 Contour Plot of the Volume Fraction of Liquid Water in the Mixture
- Figure 5.6 Contour Plot of the Volume Fraction of Vapor in the Mixture

NOMENCLATURE, ABBREVIATIONS AND ACRONYMS

1. Nomenclature (Greek Symbols)

ρ	Density
μ	Dynamic viscosity
δ	Partial derivative
Φ	Flow property per unit mass
Φ'	Fluctuation component of flow property per unit mass
Φ_m	Mean component of flow property per unit mass
λ, ϵ	Factors of the chord length
θ	Angle of revolution

2. Abbreviations (Alphabetical List)

a	Quarter of the blade chord length
c	Camber
c_{max}	Maximum camber
g	Acceleration due to gravity
H	Turbine Head
m	mass flow rate
n	Rotational speed
p	Pressure
p_m	Mean component of the pressure
p_{t1}	Total pressure at inlet
p_{t2}	Total pressure at outlet
p_{ts}	Total pressure at a section
Q	Discharge
R	Residual
S_x	Source term in the x direction

S_y	Source term in the y direction
t	Time
T	Torque
tk	Thickness of the blade
tk_{max}	Maximum blade thickness
tk_{ratio}	Blade thickness ratio
U	Velocity vector
U_m	Mean velocity vector
u	Velocity vector in the x direction
u_m	Mean component of the velocity vector in the x direction
\bar{u}'	Time average of the fluctuation component of the velocity vector in the x direction
v	Velocity vector in the y direction
v_m	Mean component of the velocity vector in the y direction
\bar{v}'	Time Average of the fluctuation component of the velocity vector in the y direction
x, y	Direction vectors

3. Acronyms

CFD	Computational Fluid Dynamics
CAE	Computer Aided Engineering
div	divergence function
grad	gradient function
k- ϵ	k-epsilon Turbulence Model
RNG	Renormalization-group
SIMPLE	Semi-Implicit Method for Pressure-Linked Equation

Keywords

CFD, RNG k- ϵ Turbulence Model, Profile-type Cavitation, Turbulence Intensity, Hydraulic Diameter, Steady Conditions, Upstream Effect

List of Software

FLUENT	Computational Fluid Dynamics Software
GAMBIT	Geometry Generating Software incorporated in FLUENT
DesignFOIL	Aerofoil Generating and Analyzing Software

CHAPTER ONE

INTRODUCTION

1.0 Background Introduction

The desire to accurately comprehend the flow features within turbines has been an area of much concern. This is a result of the need to predict their performance characteristics, determine the cavitation properties of the turbine and to further improve their efficiency. Although it is apparent that earlier studies evolved empirically and achieved satisfactory performance with minimum analytical understanding into the physics of the flow, the analysis of the basic operation with the detail knowledge of the flow behavior is, however, paramount to achieving ultimate performance. The use of force and velocity diagrams, experimentation, and dimensional analysis have helped in establishing relationships between desired flow parameters, design data and given valuable guides easing the study and the understanding of the operations of the turbine [Shepherd, 1956]¹.

With the advent of computational fluid dynamics, such study has been made easier in less time. Nevertheless, none of these approaches is yet sufficient to fully describe the turbulent nature of flow through turbines, but they depict a good account of what is really happening within the turbine and can be used for analysis [Nilson, 2002]².

The present study analyzes the flow through a Francis' turbine runner using computational fluid dynamics to describe the flow features within the runner, determine and locate the minimum pressure on the blade surface (areas susceptible to cavitation),

and to predict some performance or operating characteristics of the runner. A hypothetical exceptionally low specific speed Francis' turbine was selected in order to ensure near two dimensionality of the flow.

1.1 Objectives of the Study

The objective of the study is to analyze the flow in the runner of a very low specific speed Francis' turbine under steady conditions.

1.2 Methodology

The objective was achieved entirely with the use of FLUENT, a CFD software. DesignFOIL, aerofoil generating software, aided in obtaining the two-dimensional blade profile that was imported into GAMBIT, a geometry generating software incorporated in FLUENT, to generate the geometry. The geometry was then meshed in GAMBIT before exported into FLUENT for the CFD analysis. The study was carried under steady periodic assumption because it makes the study simple and less complex, and can give a good account of the flow features needed to achieving the objectives. The flow throughout most of the blade passage of the radial (low specific speed Francis' turbine) runner is predominantly radial, and thus the use of the two-dimensional analysis.

1.3 Scope of the Study

The study adopts the RNG $k-\varepsilon$ turbulence model for the CFD analysis since this model has gained universal acceptance for predicting results of this type of flow. The description of the flow features were limited to what was captured by the two dimensional steady periodic assumption used for the study.

CHAPTER TWO

LITERATURE REVIEW

2.0 General Introduction

Numerous studies have been carried out aiming at describing the flow features, predicting and improving the performance of hydraulic turbines using CFD, and research in this area is steadily increasing with increasing developments in CFD. Although none of these studies so far has exactly agreed with the predictions of test results throughout the entire flow domain, CFD predictions match test results in a wide flow area. Unlike experimentation, however, CFD gives further details about the flow features within the turbine and this plays a dominant role in the upgrading and modernization of existing hydraulic turbines as well as, in the design and manufacture of new hydraulic turbines. It further boosts the reliability of the design and acts as a means of proving the performance of the turbine to clients with less experimentation.

2.1 Radial Hydraulic Turbine

Radial hydraulic turbines are usually inflow type turbines with rotor blade inlet angle of 90° [Balje, 1981]³. They are low specific speed Francis' turbines. In such a turbine, fluid flows radially through the rotor vanes and exits at a smaller diameter from the turbine blades, after which it turns through 90° into the draft tube [Gorla et al, 2003]²⁴. The total operating head used in such turbines usually ranges from 30 m to 500 m [Sayers, 1990]⁴ and their diameter ratios are usually limited within the range of 2 to 2.5 [Kjolle, 2001]⁵. They have relatively low flow rates and output power, and have a flat efficiency curve [Kjolle, 2001]⁵. It has lower flexibility in its operating conditions as compared with

others in the higher specific speed range. The specific speed of radial flow turbines expressed in the form of equation (2.1) falls within 15-100 [Shepherd, 1956]¹

$$N_s = NP^{1/2}/H^{5/4} \quad (2.1)$$

Where N is rated in rpm, P in hp and H in ft

2.2 Computational Fluid Dynamics

Computational Fluid Dynamics (CFD) is the act of simulating fluid flow through objects. It enables the study of the dynamics of flowing fluids. It determines the numerical solutions of the governing flow dynamic equations to obtaining the numerical description of the flow field of interest. “In power generation, it significantly reduces the time and expense involved in designing power generation equipment, troubleshooting equipment in the field, retrofitting equipment and investigating safety-related ‘what if’ scenarios”[ASME Journal, 2001]¹³. CFD allows the building of a virtual prototype of the system to be analyzed and enables the application of real world techniques for the modeling analysis. It is completely replacing the traditional method where physical model and prototypes, along with simple rules of thumb and empirical corrections are used [ASME Journal , 2001]¹³.

Although experiments are accurate means of measuring flow properties of a system, sometimes they are very difficult, if not impossible, to be carried out. For instance in cases where the systems to be studied are under hazardous conditions, very large or required to operate beyond their normal operating limit as encountered in safety studies, the use of CFD becomes an obvious choice. Experiments can also be too costly, time consuming and/or may not be able to express further detail of great concern to the

studies. CFD is thus an essential tool and has replaced most field experimentation [Versteeg et al, 1995]¹².

The basic governing equations for CFD analysis is based on the conservation of fluid motion under given boundary conditions. For the Newtonian fluid, these equations for a two-dimensional analysis are expressed as:

$$\delta\rho/\delta t + \mathbf{div}(\rho\Phi) = 0 \quad (2.2)^{12}$$

$$\delta(\rho u)/\delta t + \mathbf{div}(\rho u\Phi) = -\delta p/\delta x + \mathbf{div}(\mu \mathbf{grad}u) + S_x \quad (2.3)^{12}$$

$$\delta(\rho v)/\delta t + \mathbf{div}(\rho v\Phi) = -\delta p/\delta y + \mathbf{div}(\mu \mathbf{grad}v) + S_y \quad (2.4)^{12}$$

Where Φ represents the change in the flow property concerned per unit mass, with \mathbf{u} and \mathbf{v} representing the instantaneous velocity components in the \mathbf{x} and \mathbf{y} direction respectively and are unknown together with the instantaneous pressure p . μ denotes the fluid viscosity while S_x and S_y denotes the source terms in the \mathbf{x} and the \mathbf{y} direction respectively.

Equations (2.2), (2.3), and (2.4) denote continuity, x-momentum, and y-momentum equations (Navier-Stokes equations) respectively.

Turbulent flow is characterized by the presence of eddying motions in a wide range of the flow. This develops fluctuations over the mean flow properties. Thus, the time dependent flow property Φ can be expressed as the sum of the steady mean component Φ_m and the time varying fluctuation component Φ' [Versteeg et al, 1995]¹². For a flow property under the two-dimensional analysis such as the velocity vector \mathbf{U}_i which is made up of \mathbf{u} and \mathbf{v} (that is the \mathbf{x} and \mathbf{y} components respectively) for instance, equations (2.2), (2.3) and (2.4) could be expressed as:

$$\delta\rho/\delta t + \mathbf{div}(\rho U_i) = 0 \quad (2.2a)^{12}$$

$$\delta(\rho u)/\delta t + \mathbf{div}(\rho u U_i) = -\delta p/\delta x + \mathbf{div}(\mu \mathbf{grad} u) + S_x \quad (2.3a)^{12}$$

$$\delta(\rho v)/\delta t + \mathbf{div}(\rho v U_i) = -\delta p/\delta y + \mathbf{div}(\mu \mathbf{grad} v) + S_y \quad (2.4a)^{12}$$

Replacing the flow variable U_i (including \mathbf{u} and \mathbf{v}) and \mathbf{p} with the sum of the mean and fluctuating component with the assumption that the effect of the density fluctuation is negligible enabling ρ to represent the mean density and taking the time average (to avoid instantaneous fluctuations) of the resulting equations, equations (2.2a), (2.3a) and (2.4a) become (the Reynolds average Navier Stokes equation):

$$\delta\rho/\delta t + \mathbf{div}(\rho U_m) = 0 \quad (2.2b)^{12}$$

$$\delta(\rho u_m)/\delta t + \mathbf{div}(\rho u_m U_m) = -\delta p_m/\delta x + \mathbf{div}(\mu \mathbf{grad} u_m) + [-\delta(\rho \bar{u}^2)/\delta x - \delta(\rho \bar{u}'v')/\delta y] + S_x \quad (2.3b)^{12}$$

$$\delta(\rho v_m)/\delta t + \mathbf{div}(\rho v_m U_m) = -\delta p_m/\delta y + \mathbf{div}(\mu \mathbf{grad} v_m) + [-\delta(\rho \bar{u}'v')/\delta y - \delta(\rho v'^2)/\delta x] + S_y \quad (2.4b)^{12}$$

Where equation (2.2b) is the continuity equation and equation (2.3b) and (2.4b) is the Reynolds equations. The additional unknowns (\bar{u}' , $\bar{u}'v'$, v') within the Reynolds stresses ($\rho \bar{u}'^2$, $\rho v'^2$ – normal stresses, $\bar{u}'v'$ – shear stress) in the Reynolds equations makes the available equations less than that required to determine the unknowns thus the need of turbulence modeling, which develops computational procedures of sufficient accuracy and generality to enable the predictions of the unknowns (achieve a ‘closure’ for the unknowns) [Versteeg et al, 1995]¹².

The turbine head H_T can be estimated as:

$$H_T = (p_{t1} - p_{t2})/\rho g \quad (2.5)^{15}$$

$$\eta_h = Tn/Q(p_{t1}-p_{t2}) \quad (2.6)^{15}$$

where p_{t1} and p_{t2} denote mass weighted average of total pressure at inlet and total pressure at exit of the turbine respectively. The numerator and the denominator of equation (2.6) is the power output and the power input to the turbine respectively.

2.3 Numerical Investigation and Validation of Flow in Hydraulic Turbines

Computational fluid dynamics is tool mostly used in the study, development and the design of hydraulic turbines. Steady state CFD analysis has been a validated and an integral part of hydraulic turbine design.

Nilsson et al [6] in their research to investigate and validate flow in the GAMM Francis turbine using the CFD Code CALC-PMB observed that there were great similarities between experimental and numerical predictions. The study assumed a periodic and a steady flow with the computational domain consisting of a single runner blade under the periodic condition. This investigation was done at the best efficiency and some off-design operating conditions. The simulation qualitatively captured most flow features, however, some noticeable discrepancies at low mass flow rate and at areas where recirculation and unsteadiness dominates the flow were observed. The study also observed some uncertainties when comparing the predictions quantitatively and this was attributed to uncertainty in some measurements. The study argued that the steady periodic CFD assumption can be used for water turbine computations but might not be able to capture all flow features [Nilsson et al, 2001]⁶. Dai et al [21] in the study of the internal flow through a radial turbine using a steady three-dimensional Reynolds averaged Navier-Stokes solver (BTOB3D) for the numerical analysis observed that the CFD captured most

of the characteristics of the flow and further confirmed the excellent qualitative agreement to experiment. Quantitative accuracy was observed at certain flow region with the incidence angle having less effect on the core flow characteristics at constant speed line. The inlet and the outlet conditions however plays a key role in the predictions of the CFD [Dai et al, 2004]²¹. In another study, Guedes et al [10] assuming periodic condition of 1 runner channel and 4 stator channels to represent 5 runner and 22 stator channels stimulated both steady and unsteady rotor- stator analysis of a hydraulic turbine using both experimental and CFD approach. The study also investigated the stator-rotor computational capabilities of the Fine Turbo and CFX-TASCflow CFD codes. It showed the strong dependence of continuity or consistency to mesh refinement at both sides of the stator-rotor interface. In other words, the refinement and the consistency of the mesh at the stator-rotor interface strongly affected the computational capability of both codes. Also, both analyses proved that the stator-rotor models were fully conservative and capable of producing the flow conditions encountered in the stator-rotor interaction zone of a hydraulic turbomachine. Increasing shock effects (sudden pressure rise/jump) in the flow field at the blade leading edge were observed at low flow rates. The overall results showed that the unsteady stator – rotor computation was able to accurately predict the flow behavior at the stator-rotor interaction zone, as it displayed qualitatively the same flow features found by measurements and indicated the way the instability of machine was induced. All stator-rotor interaction effects such as potential and viscous effects were accurately expected to be reproduced with unsteady analysis of the stator-rotor interaction [Guedes et al, 2002]¹⁰. Ciocan et al [11] under the same study revealed that the steady numerical calculations show relatively good qualitative agreement if the flow

angle at outlet of the rotor is more or less adapted to the draft tube entrance angle. The unsteady computation gave a good prediction of the mean flow behavior except in some areas where deviations of about 32% were observed which was as attributed to the coarse mesh in that region [Ciocan et al, 1998]¹¹.

Similar study was done to predict the unsteady wicket gate-runner interaction in a Francis' hydraulic turbine at GE Energy Hydro. Nennemann et al [9] presented a method of stimulating unsteady flow field resulting from rotor-stator interaction with CFD. Validation of predictions was done using unsteady pressure measurements on a model scale runner. CFX-5 CFD software with the k- ϵ turbulence model was employed in the analysis. The study observed the impossibility of using unsteady periodic rotor simulation with single wicket gate and single runner channel as used in steady state for the analysis of rotor interface since there are always unidentical number of wicket gate and blades in any Francis' turbine. However, in order to reduce the meshing size and calculating time, the study employed some combination for the analysis while maintaining an identical periodicity on both wicket gate and runner mesh. For instance, a combination of 7 wicket gate channels and 5 runner channels was deemed suitable to periodically analyze a 24 wicket gates and 17 blades Francis' turbine. The study observed that dynamic torque predictions have some dependence on the mesh size. While acknowledging that there is stator- rotor interactions in all hydraulic turbines within a certain level, pressure fluctuations however became significantly large relative to the stress levels in medium to high head hydraulic turbines. This was due to the high wicket gate outlet velocity in such turbines and the small radial gap between the blade rows. The predictions showed

excellent qualitative agreement with test characteristics curves with large deviations occurring near the leading edge where very high amplitude gradient were present. Insufficient mesh resolution was attributed to be the cause of the deviations. Average deviations within 3 to 10% were observed. Further mesh refinement achieved accuracy of approximately less or equal 20% [Nennemann et al, 2005]⁹.

Drtina et al [7] stimulated the turbulent flow in the complete Francis hydraulic turbine under steady conditions using 3D Euler code with the k- ϵ turbulence model and also observed astonishing accuracy (over 90% accuracy) with model test even at operating points far from the best points. Predictions showed good agreement at different guide vanes openings except at very large values of circumferential velocity corresponding to low heads that deviation between efficiencies were high. This was attributed to the highly unsteady nature of the flow at these operating points. There were also some amount of inaccuracy in the exact predictions of efficiency level and was attributed to the choice of turbulence model and the grid refinement. The study estimated it to be varying within +/- 2 % in absolute efficiency level [Drtina et al, 1997]⁷. To further improve this research, Ruprecht et al [8] conducted an unsteady simulation of an entire Francis' turbine without the use of periodicity using parallel computing with non-matching sliding meshes as a means of coupling between different components while employing dynamic boundary conditions. Domain decomposition and the application of parallel solver for the linear systems of equations were used for parallelizing each component. The simulation showed clearly the reduction of pressure from the spiral casing to the runner outlet with the runner inlet stagnation point occurring at the leading edge. However, coarse mesh

was employed in the simulation to save computational effort and cost, and this resulted to an early equalization of the wakes obtained behind the blades and shortened the time required to obtaining vortex rope as in model tests. However, the study was a feasibility study rather than for obtaining and validating quantitative results [Ruprecht et al, 2000]⁸.

It is believed that 40% of the hydraulic turbine performance or three quarter of the overall pressure recovery can be obtained from the draft tube [Susan-Resiga et al, 2005]¹⁸, thus other studies were aimed at analyzing the swirling flow which occurs at the exit of the runner. Swirling flow at the exit of the runner mitigates flow detachment at the cone of the runner but also comes along with flow instabilities leading to surge in the draft tube [Susan-Resiga et al, 2004]¹⁶. This introduces complexity in the flow as a result of curvature effects and the adverse pressure gradient caused by the diffuser as the runner generates swirling flow at the exit. The standard k- ϵ turbulence model does not produce very good predictions with such flows yet it is still the most widely used approach for engineering applications [Mauri et al, 2000]¹⁷. This is because of its ability of producing good results in a wide flow domain encountered in most engineering application. Susan-Resiga et al [16] in their studies on the swirling flow downstream of a Francis turbine runner using a superposition of three various vortex flow to accurately represent the swirling flow observed that the swirling flow configuration at the outlet of the Francis turbine runner had major influence on the overall behavior of the flow downstream in the draft tube. It recommended the avoidance of reaching critical state of swirl at runner outlet within the normal operating range in the design and optimization of turbine runners [Susan-Resiga et al, 2004]¹⁶. Mauri et al [17] studied the influence of boundary

conditions on the numerical predictions of the flow at the exit of the runner using CFX-TASCflow 2.9 with the k- ϵ turbulence model coupled with logarithmic wall functions. The studies showed the global performances of the draft tube as a function of the flow rate; the evolution of axial velocity component at the immediate exit of the runner was characterized by the decreasing importance of the low velocity zone at the centre of the draft tube caused by the presence of high swirl for low flow rates, and that reverse flows were only observed at higher flow rates. The study also observed that, a lower inlet turbulent dissipation rate led to a failed prediction of the reserve flow zones causing an overestimated recovery factor and this was attributed to the difficulty of standard k- ϵ model in predicting swirling flows and the use of extrapolations for inlet profiles [Mauri et al, 2000]¹⁷.

2.4 Challenges and the Future of CFD Analysis of Hydraulic Turbines

The design of almost all hydraulic machines and turbomachines to be general is unthinkable without the incorporation of CFD [FLUENT User Guide, 2005]¹⁵. Although CFD is currently the most widely used technology for flow analysis in hydraulic machines, it has some defects having to do with the selection of the right turbulence model which accurately describes the entire flow feature throughout the entire unit. Unsteady state modeling provides quite an accurate solutions for complex flow however, it require much computational cost and time, making most analysis to be done in steady state. Besides, CFD faces a lot of challenges especially in the aerospace and marine sectors where there have been recorded frustrations of turbulence modeling, its accuracy of stimulating transient phenomena fundamental to viscous flows and/or the inadequacies

of background meshes to resolve the intricacies of small-scale effects [Annual Conference of CFD, 2005]¹⁴.

There are wide ranges of CFD software and techniques to handling flow problems, however, none can be categorized to be generally acceptable for some specific flow features, for all flow conditions or can exactly predict turbulence modeling problems. Each has some inherent defects which are being addressed with time. It is hoped that one technique would emerge which would handle most of these uncertainties as well as to incorporate more automation to enable the detection and repairs of geometries in CFD models [FLUENT User Guide, 2005]¹⁵. With the increasing technological advancement especially in improving the performance of computing hardware, CFD might completely replace experimentation in the near future.

2.5 Some Successful Applications of CFD Analysis

CFD have successfully been applied to a lot of heat transfer problems, the field from which the technique originated. It has made dramatic impact in the performance of aircraft engines, steam, hydraulic and gas turbines for power generation. For instance, it brought great improvement in predicting efficiencies and aerodynamic loading range of aircraft engines. One successful problem solving applications of CFD was the problem associated with vortex shedding at the inlet of a low head power plant using two identical bulb turbines. One of the two turbines (inner turbine) experienced severe bearing problems when it was in operation. CFD investigation depicted clearly the vortices shedding from the inlet towards downstream to the inner turbine explaining the reason behind the bearing destruction. From this observation, a modified geometry was

suggested, modeled and verified with CFD to ensure that the problem never existed before finally reinstalling this modified unit [Ruprecht, 2000]²⁰ and it proved to be successful in solving the problem completely.

CHAPTER THREE

MODELING

3.0 Introduction to FLUENT

FLUENT is one of the commonly used CFD software in fluid flow analysis. It allows fluid flow simulation in a wide range of areas and has a wide range of geometry tools. In handling dynamic and moving mesh, it has the sliding mesh and multiple reference frames models which have been proved to be effective and fully compatible with other models. It is user-friendly and robust. It is able to coordinate with other geometry generating software, and this extends its capability to generating different type of meshes with its unstructured grid technology (quadrilateral and triangular for 2D simulations; and hexahedra, tetrahedra, prisms and pyramids for 3D simulations) . It incorporates adaptive meshing technique which widen its range in working with most models. It is fast and reliable. FLUENT offers GAMBIT and TGrid for building geometry and volume meshing (pre-processor). GAMBIT also reads CAD files and conditions any imported CAD geometry for the numerical analysis (Solver). The solver of FLUENT employs the finite volume method, a development of finite difference stream of numerical solution technique. The post-processor of FLUENT generates meaningful graphics, animations and reports to convey the results from the solver, as well as allowing its solution data to be exported where necessary to other CFD or CAE packages for additional analysis [FLUENT User Guide, 2005]¹⁵.

This present analysis used the RNG k- ϵ turbulence model, one of the numerous turbulence models available in FLUENT. It is a development of the standard k- ϵ

turbulence model of Launder and Spalding [FLUENT User Guide , 2005]¹⁵.

3.1 k-ε Turbulence Model

The k-ε turbulence model, just like other turbulence models employs the Reynolds-average Navier Stokes equations and is the most widely used turbulence model in engineering applications. It focuses on factors that affect turbulent kinetic energy. It performs well in confine flows where the Reynolds shear stresses are essential [Versteeg et al, 1995]¹². It is a two-equation turbulence model which solves two separate transport equations to allow the independent determination of turbulent velocity and length scale (dissipation rate or ε) [FLUENT User Guide, 2005]¹⁵. The turbulence kinetic energy k determines the energy in the turbulence while the turbulence dissipation ε determines the scale of the turbulence as it is transported.

In FLUENT, it comprises of three forms; Standard, RNG, and the Realizable k-ε turbulence model, each having a formulation to handle the different physics of flow problems encountered in CFD analysis. They are modified version of each other to allow predictions of flow properties under certain flow type such as low or high Reynolds number flow. The standard k-ε turbulence model is used for high Reynolds number flow and it makes use of the universal behavior of near wall flows to avoid the need of integrating the model equations through the wall within a condition such that, the mean velocity at a coordinate direction y_p normal to the solid wall satisfies the log-law for viscous layers in the range $30 < y_p^+ < 300$. However, at low Reynolds number the log-law becomes invalid constraining the application of the standard k-ε model. To overcome this

constraint, wall damping have been applied to enable the viscous stresses overcome the turbulent Reynolds stresses [Versteeg et al, 1995]¹².

The RNG k- ϵ turbulence model, a modified form of the standard k- ϵ model uses analytically derived differential formula for the effective turbulence viscosity to account for the effect of low-Reynolds number. It also has additional terms in the length scale equation which improves CFD predictions for cases of strained and swirling flows [FLUENT User Guide, 2005]¹⁵, hence it was adopted for this study.

The realizable k- ϵ turbulence model, a further modification of the standard k- ϵ turbulence model has another formulation for the turbulent viscosity and a transport equation for the length scale (ϵ) (the dissipation rate) to satisfy certain mathematical constraints consistent with the physics of the turbulent flows on Reynolds stresses. It accurately predicts the spreading rate of both planer and round jets flows. However, it produces some non-physical turbulent viscosities in cases where there are both rotational and stationary flow domains as in multiple reference frame formulation [FLUENT User Guide, 2005]¹⁵, thus it was not employed for this study.

3.2 CFD Modeling of the Francis' Turbine Runner

3.2.1 Boundary Conditions

1. Inlet Boundary Condition: Three inlet boundary conditions can be used in describing the flow property at inlet to the casing. These are velocity inlet, total pressure inlet, and mass flow inlet boundary condition. The velocity inlet boundary condition was used for the present simulations. This was because the

fluid (water in this case) is incompressible (constant density) as such the use of the velocity inlet boundary conditions eliminates the use of the mass flow inlet boundary condition. Besides, the use of velocity inlet allows the easy variation of the flow direction and magnitude which was to be used for the analysis.

In defining the velocity at inlet for the CFD analysis, the velocity magnitude and direction was used to accommodate the different angles of the guide that will be used for the analysis. And in specifying the reference frame for the velocity specification, the “relative to adjacent cell zone” was used for ease of convergence.

2. Outlet Boundary Condition: Atmospheric pressure conditions were assumed at the outlet of the model thus pressure outlet boundary condition was used as the boundary condition at the exit.

Zero gauge pressure was assigned at the outlet and the backflow specification method used to define the pressure was the normal to boundary since the flow was assumed to exit at an angle of 90 degree to the boundary. The backflow specification method was assigned so that should a relevant flow be pulled in (re-enter the computational domain) through the outlet into the computation, that value would be used. However, if such a condition does not occur throughout the computation, that value is ignored by FLUENT. This can occur in cases where there are flow re-circulation at the exit.

3. Wall Boundary Condition: The single blade in the passage was set to be a rotating wall relative to the part of the rotor encompassing it (working fluid) based on the rotating reference frame formulation. The standard wall functions were used to solve the viscous flow layer over it and adaptation was enforced on the adjacent nodes to move them into conformity to that required by the adopted standard wall functions. Figure 2 displays the model after adaptation.
4. Periodic Boundary Condition: The two adjacent edges connecting the inlet and the outlet were set to be cyclic periodic.

Figure 3.1 and 3.2 below respectively describes the edges the various boundary conditions were assigned and the grid after adaptation.

Figure 3.1 Display of the Model and the Allocation of Boundary Condition

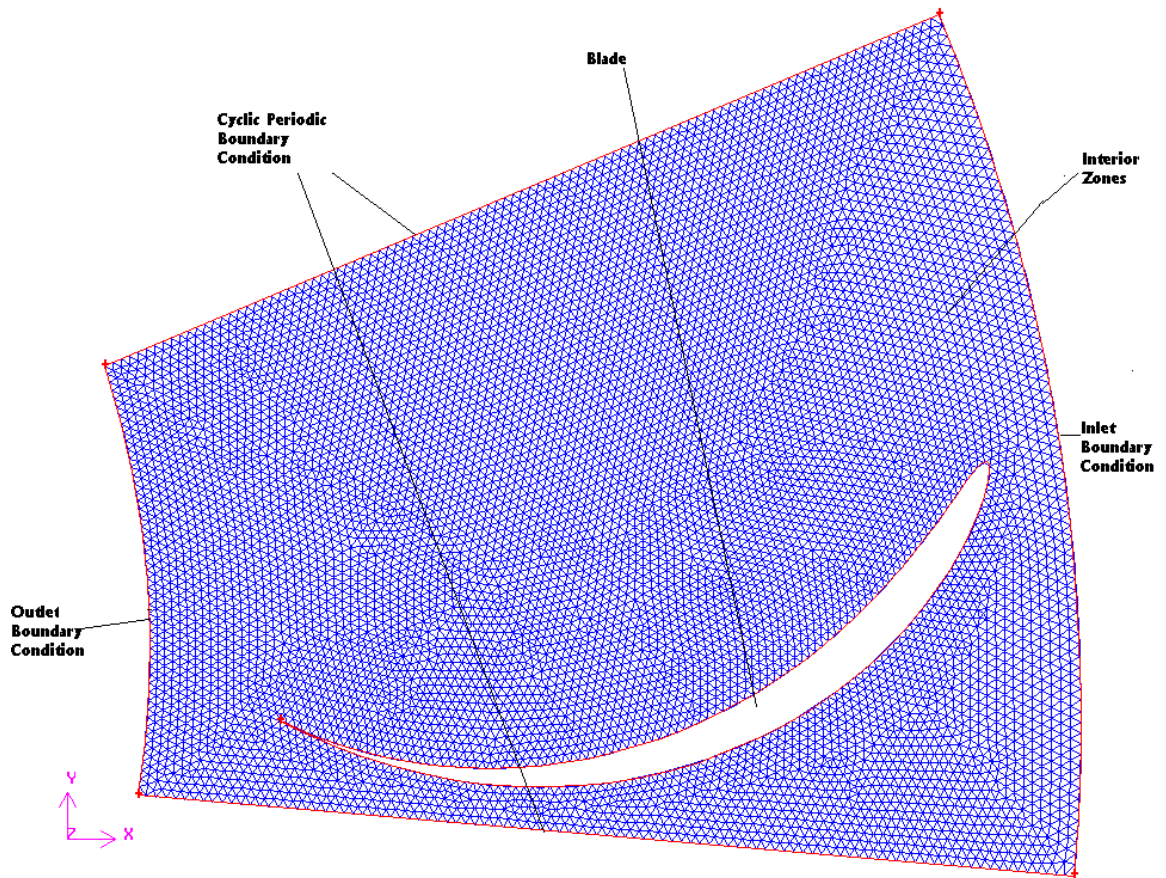


Figure 3.2 Grid Display of the Model after Adaptation

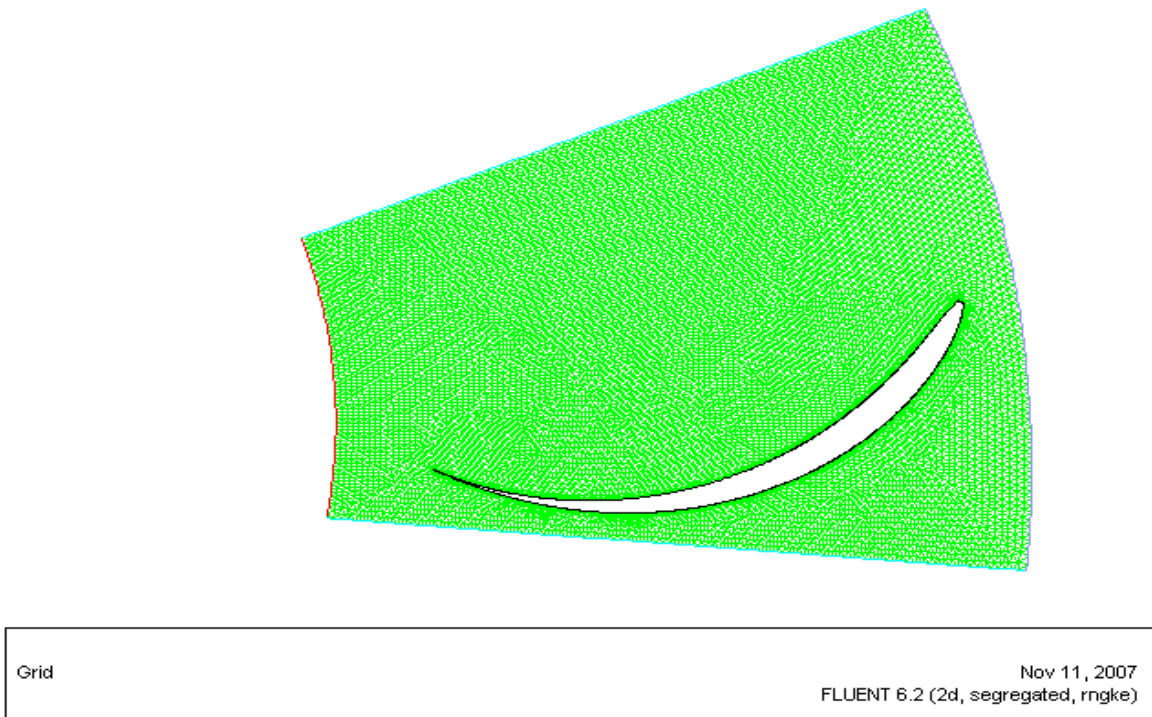


Figure 3.2 shows the grid display after the near wall adaptation of the grid based on the y^+ formulation. The change in the meshing structure around the surface of the blade due to the adaptation is clearly depicted from this figure.

3.2.2 Specification of Turbulence Parameters

The turbulence specification method used to describe the inlet boundary condition was turbulence intensity (for the turbulence kinetic energy k) and hydraulic diameter (for the length scale from which the turbulence dissipation rate ϵ is calculated). This was because their value can easily be estimated and are commonly used specification in describing flow in hydraulic turbines. The hydraulic diameter was assumed to be the mean diameter of the rotor and the value of the turbulence intensity was an intermediate of the two

extremes of turbulence. The turbulence intensity was set to 7% (that is, between 1-5% considered for low turbulence and 10% and beyond for high turbulence flow).

Turbulence intensity between 5-10% was assumed sufficient to represent the fully developed turbulence experienced within this unit [FLUENT User Guide , 2005]¹⁵.

3.3 Specification of the Francis' Turbine Runner

The following values were assigned to the Francis' turbine runner used for the study.

Turbine Blade Speed ~ 115.4 rpm

Number of Blades ~ 13 of which only one (1) was used for the periodic model

Blade Alignment (at inlet relative to its tangent at exit) ~ 20 degree

These values were obtained based on the operating specification of a similar runner. A blade speed of 76.9 and 173.1 rpm was also used for the analysis. The choice of these values was arrived at based on a scaling factor used on page 28-29 of the Lecture Handout on the Design of Francis Turbine [Lecture Handout, 2006]²⁶. In specifying the rotational velocity of the blade in FLUENT using the rotating frame formulation, the fluid was set to be rotating at the assigned speed relative to the blade. Guide angle ranging from between 20 to 80 degree with inlet velocity ranging from 20 to 40 m/s at interval of five were used for the analysis.

3.3.1 Blade

The specifications used to obtain the blade on DesignFOIL were as follows:

Camber Parameter ~ 0.4

Thickness Parameter ~ -0.04

Percent Thickness ~ 5.12

Mean Diameter ~ 3.5 m

The Joukowski approach generates its aerofoil by mapping a circle onto a complex plane. The camber parameter describes how much camber the aerofoil possesses. It refers to the y-coordinate from the centre of the circle. The thickness parameter describes the thickness of the aerofoil. It refers to the x-coordinate from the centre of the circle; while the percentage thickness gives an estimate of the maximum aerofoil thickness as a percentage of the chord length [User Guide, Trial Edition of DesignFOIL, 1990-2000]²⁵. They are all dimensionless parameters. For an arbitrary point within the circle at a co-ordinate $(\lambda a, \epsilon a)$, with $4a$ is the chord length of the blade, tk denoting the thickness of the blade, c the camber, and θ being the angle of revolution;

$$tk = 4 \epsilon a (1 - \cos \theta) \sin \theta \dots\dots\dots(3.1)$$

$$tk_{\max} = 3 \sqrt{3} \epsilon a \text{ at } \theta = 2\pi/3 \dots\dots\dots(3.2)$$

$$tk_{\text{ratio}} = 3 \sqrt{3} \epsilon a / 4a \approx 3 \sqrt{3} \epsilon / 4 \dots\dots\dots(3.3)$$

$$c = 2 \lambda a \sin^2 \theta \dots\dots\dots(3.4)$$

$$c_{\max} = 2 \lambda a \text{ at } \pi/2 \dots\dots\dots(3.5)$$

3.4 Meshing, Solver and the Convergence Criteria

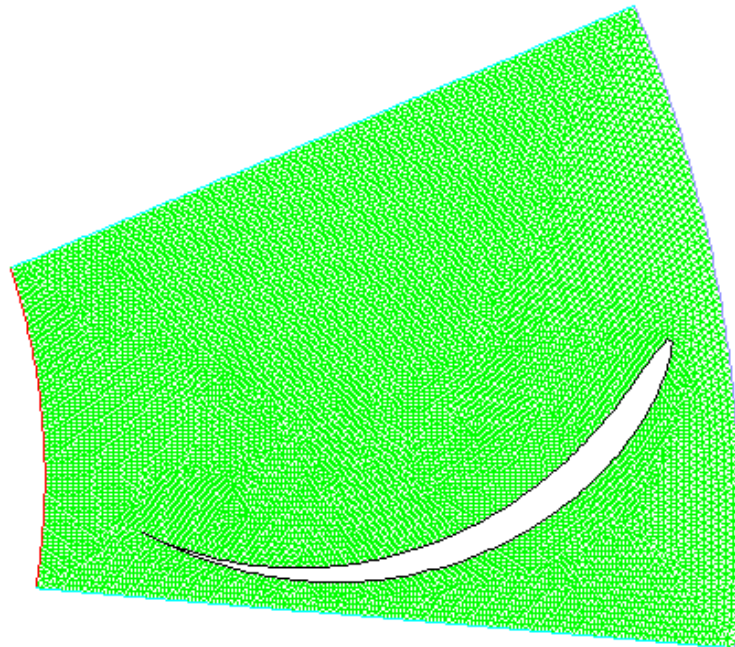
3.4.1 Meshing

An unstructured meshing comprising of triangular grids was used for meshing the entire area model. Figure 3.3 shows the gambit model of the turbine. The study employed the standard wall functions for the near-wall treatment of the flow (incorporate the effects of viscous layer near the wall into the prediction of turbulence properties near the wall).

The near wall grids were ensured to fall within the range stipulated by the log-law of

viscous layer ($30 < y^+ < 300$). In other words, the nodes on the edge and area mesh by the walls were spatially moved such that they fell within the range of the y^+ required for the standard wall function used, while ensuring that no area elements were inverted to negative value in the process. Conformity was ensured, and the number of mesh nodes and nodal connectivity also remained unchanged around the wall zones [Burgreen et al, 2001]¹⁹

Figure 3.3 Grid Display of the Periodic Model



Grid	Nov 15, 2007 FLUENT 6.2 (2d, segregated, rngke)
------	--

Grid Information:

Total Number of Cells ~ 21803
Total Number of Faces ~ 33443
Total Number of Nodes ~ 11740

3.4.2 The Solver and Turbulence Model

The segregated solver was employed for the CFD analysis, instead of the coupled solver available in FLUENT to save storage and computational time. It solves one flow property for each cell at a time. The RNG turbulence model together with the default SIMPLE algorithm and the second order upwind discretization scheme was used for the CFD analysis. The RNG k- ϵ turbulence model is very accurate, robust and reliable for a wide range of turbulent flows, and converges relatively easy under the steady flow state assumed. It is also able to handle flows with low-Reynolds number just as in the case of the turbine under study and can be applied to swirling flows which is usually encountered within the flow domain of a turbine. The SIMPLE algorithm produces satisfactory corresponding pressure and velocity fields with savings in computational effort due to improve and fast convergence rate. The second order upwind interpolation scheme minimizes false diffusion errors and produces more accurate solutions [Versteeg et al, 1995]12. The default standard discretization scheme was however maintained for the pressure interpolation. The flow features associated with the rotating part of the unit were analyzed using the rotating reference frame capability. This was because the rotating reference frame can be included in single domain and also allows flow field independent of the orientation of the moving part. It is also compatible with the turbulence model adopted. The fluid was set rotating at the blade speed relative to the blade. Steady conditions were assumed to prevail.

3.4.3 Convergence Criteria

Convergence was judged by examining both residual level and net mass imbalance, since residual alone can be misleading for some classes of flow phenomena. The criteria for convergence of residual for all turbulence property was at least 0.001 while the mass imbalance was limited to 0.02 kg/s. The residual R^Φ for a general variable Φ computed by the segregated solver adopted for the study is expressed as:

$$R^\Phi = \frac{\sum_{\text{cells}} P \left| \sum_{\text{nb}} a_{\text{nb}} \Phi_{\text{nb}} + b - a_P \Phi_P \right|}{\sum_{\text{cells}} P \left| a_P \Phi_P \right|} \dots\dots\dots (3.6)^{15}$$

Where a_P is the center coefficient, Φ_P is the general variable at a cell P, a_{nb} are the influence coefficients for the neighboring cells, and b is the contribution of the constant part of the source term. The default under relaxation factors for the various flow and turbulence properties (pressure~0.3, density~1, body forces~1, momentum~0.7, turbulence kinetic energy~0.8, dissipation rate~0.8 and viscosity~1) were maintained for the single phase predictions. However, in running the multiple phase analysis to predict the results for cavitation, these relaxation factors were reduced to enable the solution to converge.

CHAPTER FOUR

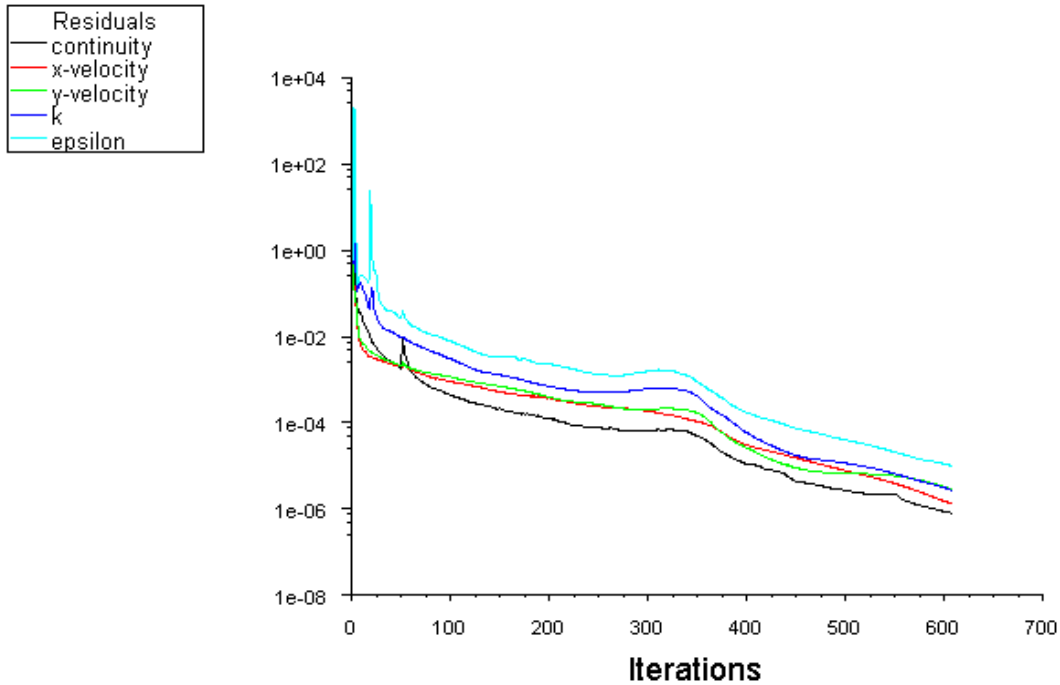
SINGLE PHASE BLADE TO BLADE FLOW ANALYSIS

4.0 Results and Discussion for Single Phase Analysis

This section presents results of the blade-to-blade flow analysis of the radial flow in the Francis' turbine without the consideration of cavitation (single phase analysis). The analysis was done for cases with varying inlet flow velocity from 20 to 40 m/s at intervals of 5 m/s and also for three different rotational speeds of 76.9, 115.4 and 173.1 rpm. For each of the inlet velocities and rotational speeds the relative flow was directed at angles of 20, 25, 30, 35, 40, 45, 50 and 55 degree with the radial direction at the inlet boundary. Relative flow refers to the flow associated with the relative velocity, that is, velocity relative to the rotating runner.

Figures 4.1 to 4.5 below show the convergence history of the solution, the static contour, absolute velocity, relative velocity and total pressure distribution for the case with an inlet velocity of 25 m/s and inlet flow angle of 45 degree while Figures 4.17 to 4.20 show the corresponding plots for that with an inlet velocity of 40 m/s and inlet flow angle of 60 degree.

Figure 4.1 Convergence History at Inlet Velocity of 25 m/s and an Inlet Flow Angle of 45 degree



Scaled Residuals Sep 19, 2007
FLUENT 6.2 (2d, segregated, rngke)

Convergence was achieved after 608 iterations with a residual value set to 0.00001.

Mass Imbalance ~ 0.0020 kg/s (about 8.5×10^{-6} % of the mass flow rate at inlet)

Total Gauge Pressure inlet based on the Mass Weighted Average ~ 2.0455 MPa

Total Gauge Pressure Outlet Based on the Mass Weighted Average ~ 1.4948 MPa

Figure 4.1 shows the convergence history of the solution after 608 iterations for the case with inlet velocity of 25 m/s directed at 45 degree to the radial direction. Convergence of residuals was achieved with residual monitoring criteria set to 0.00001. The total gauge pressure at inlet was much higher than that at outlet which shows that the blade extracts some energy from the flow.

Figure 4.2 Contour Plot of Static Pressure Distribution at Inlet velocity of 25 m/s and an Inlet Flow Angle of 45 degree

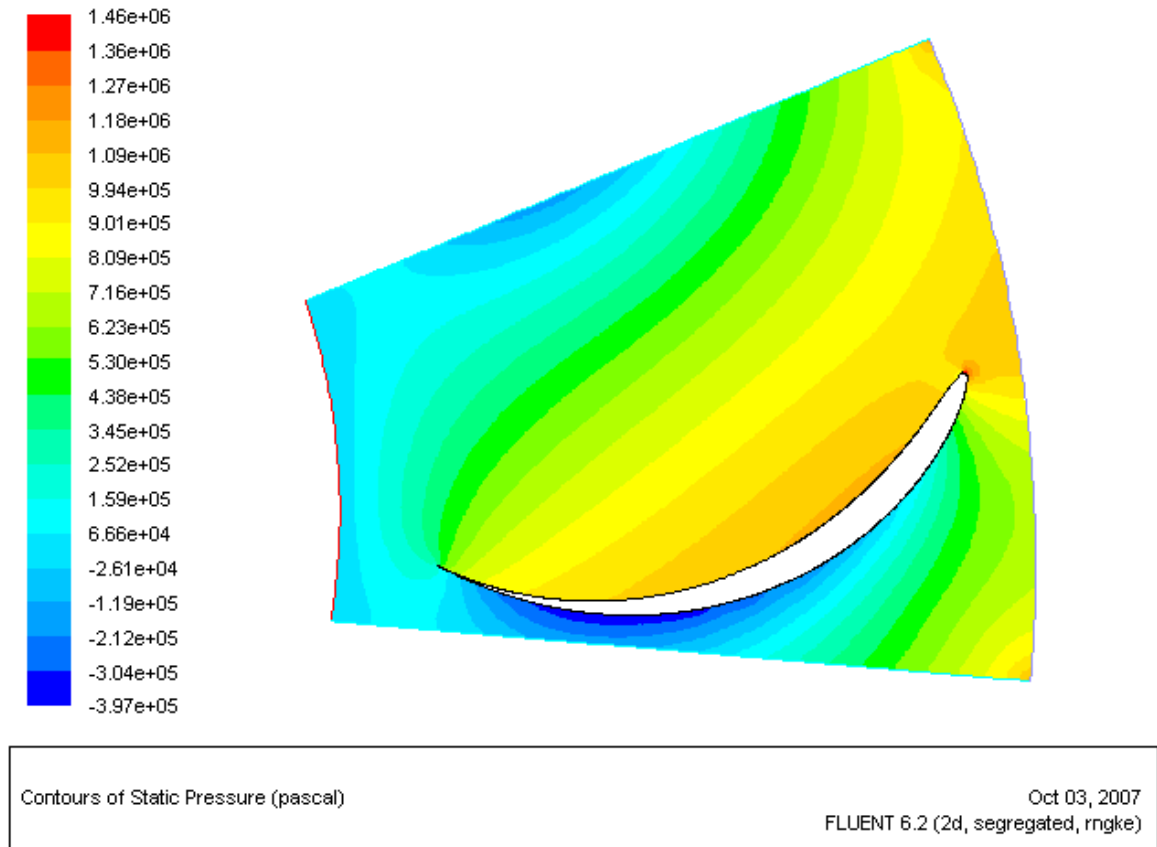


Figure 4.2 shows the static pressure contour plot for an inlet flow velocity of 25 m/s at 45 degree to the radial direction. The plot shows negative pressures of higher magnitude than the operating atmospheric pressure used for the study at some sections of the flow domain and this indicates cavitation. This will lead to mass transfer from the liquid phase to the vapor phase. This mass transfer when incorporated in the solution will enable the pressures to remain positive throughout the domain. Unfortunately, no provision of this mass transfer can be made with the single phase modeling used for the study, thus the non-physical negative pressures in the solution. From the predictions of

the minimum pressures as observed in Tables 1 to 5, these negative pressures were observed for all the cases which imply that cavitation occurred in each of the cases. Nevertheless, the plot generally shows the reduction of pressure as fluid flow from the inlet to the exit. The pressure at the pressure side of the blade was also higher than that at the suction side. There were traces of high pressures at the stagnation points (inlet tip) of the blade. The drop in pressure observed at the back of the blade during the runner operation was also noticeable. These are normally areas where the onset of profile-type cavitation is usually observed.

Figure 4.3 Absolute Velocity Vector Plot at Inlet Velocity 25 m/s and an Inlet Flow Angle of 45 degree

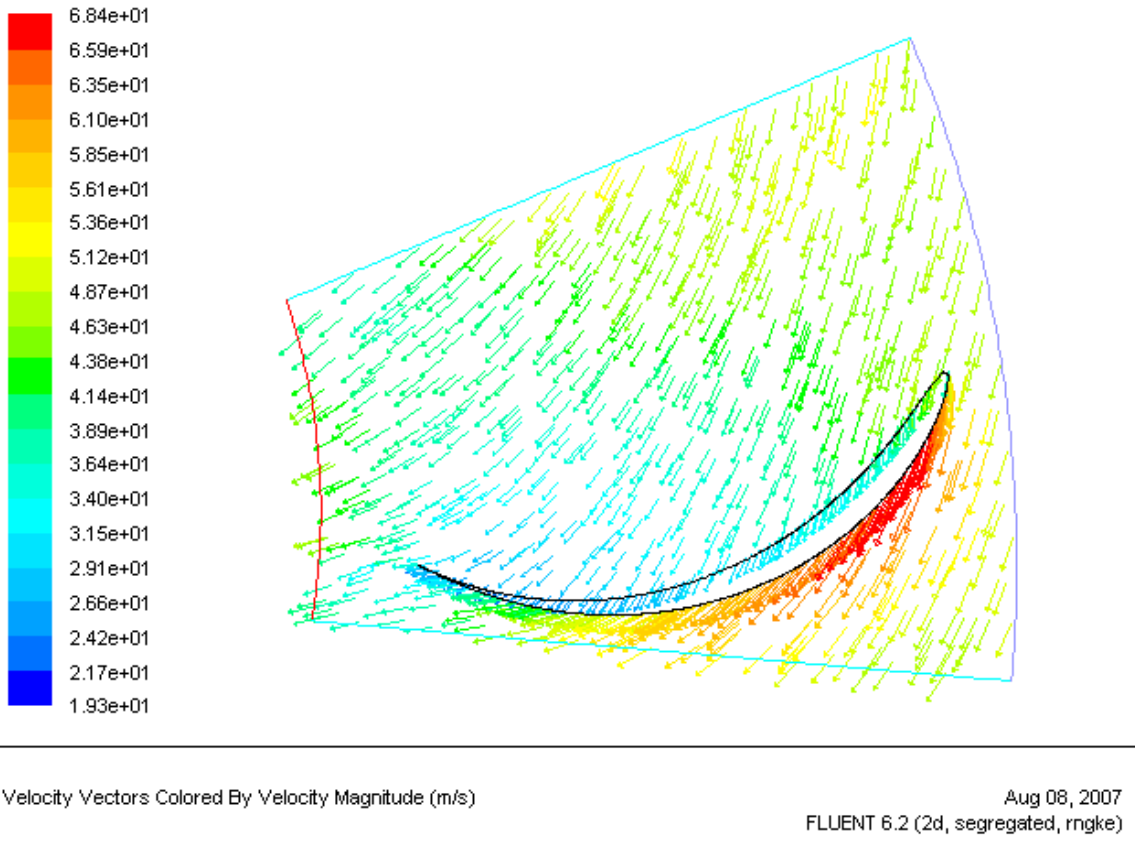


Figure 4.3 shows the absolute velocity vector plot for an inlet flow velocity of 25 m/s at an inlet flow of 45 degree. The velocities at the exit were quite lower as compared to that at inlet. The results also depict clearly the higher velocities at corresponding points on the suction side of the blade as compared to the pressure side with the flow hitting the pressure side of the blade.

Figure 4.4 Relative Velocity Vector Plot at Inlet Velocity of 25 m/s and an Inlet Flow Angle of 45 degree

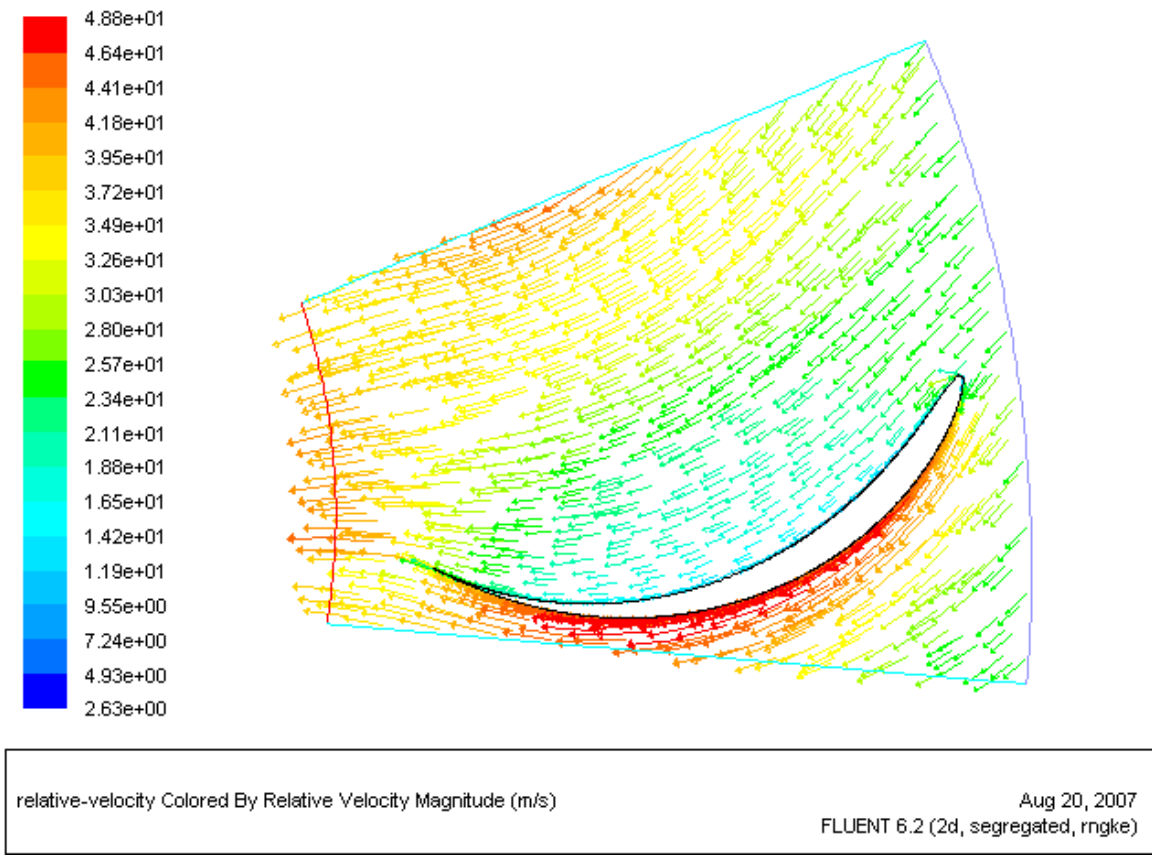


Figure 4.4 shows the relative velocity vector plot for an inlet flow velocity of 25 m/s directed at 45 degree to the radial direction. The relative velocity was predicted with

respect to the rotating fluid (flow area enclosing the blades). The relative velocity was also generally higher at the suction side of the blade than the pressure side. This accounts for the high static pressures observed at the pressure side.

Figure 4.5 Contour Plot of Total Pressure Distribution for the Case with Inlet Velocity of 25 m/s and an Inlet Flow Angle of 45 degree

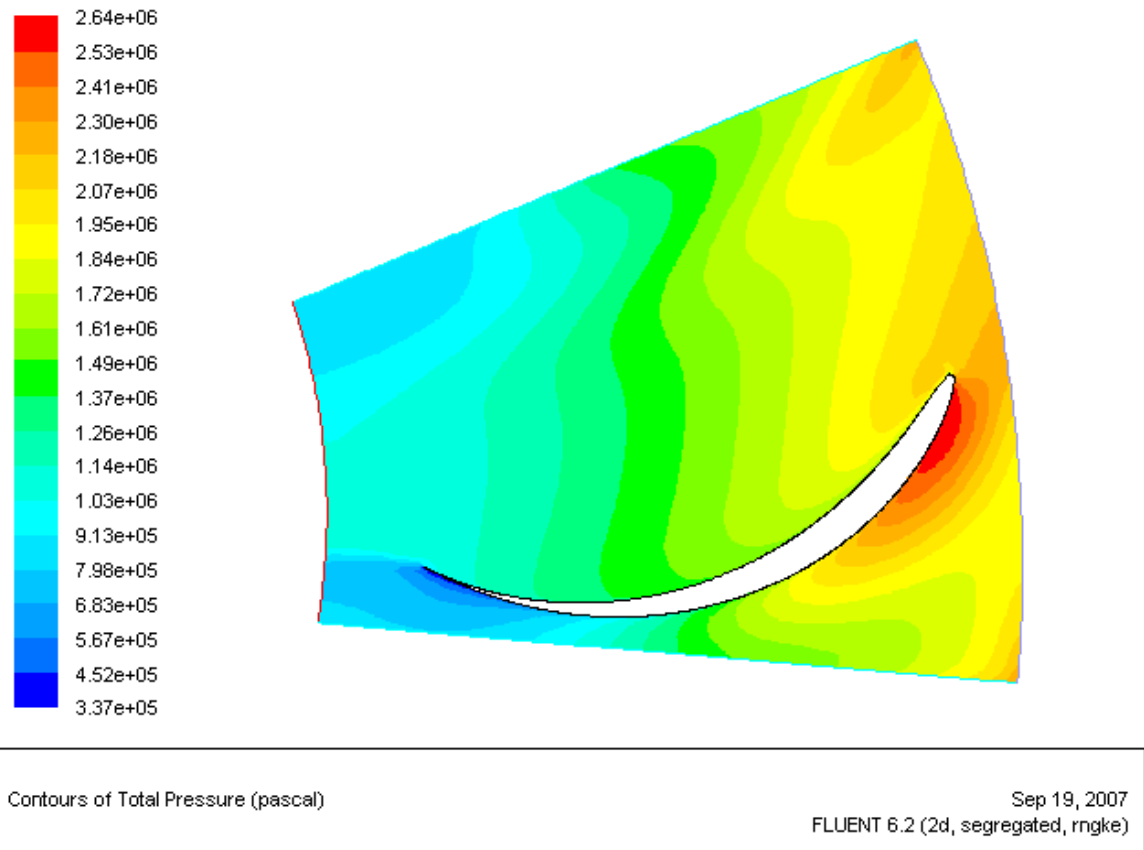
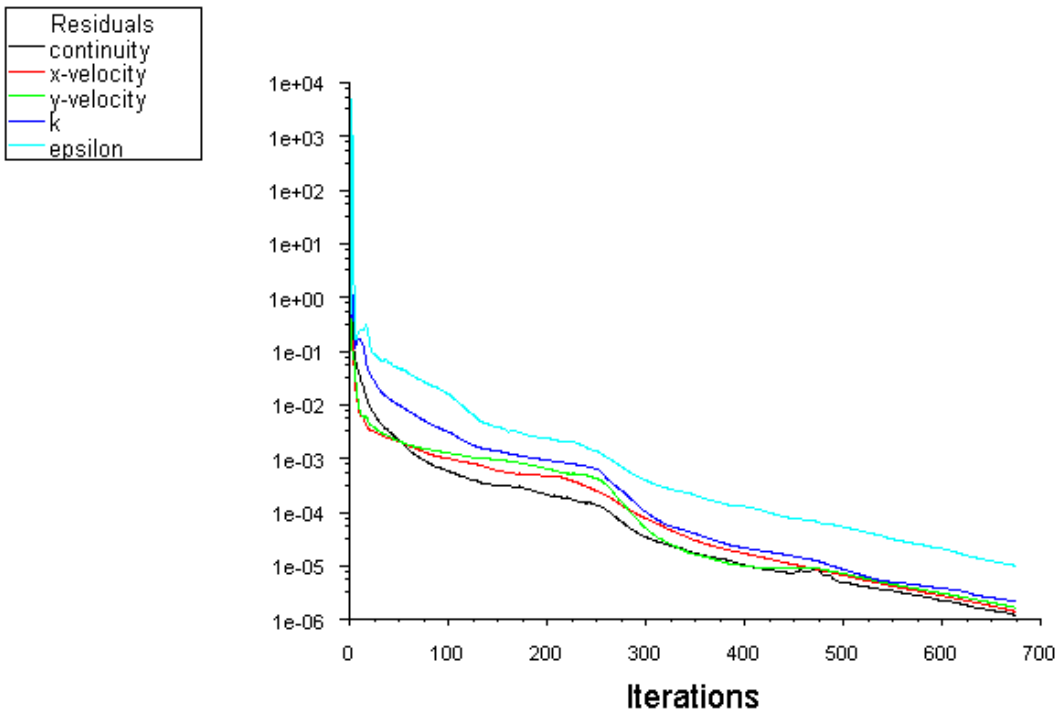


Figure 4.5 above shows the total pressure distribution for inlet flow velocity of 25 m/s directed at 45 degree to the radial direction. The total pressure drops from the inlet to the outlet as expected for a turbine. The blade extracts this energy from the fluid. The pressure drop that occurs at the back of the blade was also observed.

Figures 4.6 to 4.9 show the convergence history, static pressure contour plot, absolute velocity and relative velocity vector plot for the case with the inlet flow angle of 60 degree and an inlet velocity of 40 m/s.

Figure 4.6 Convergence History at Inlet Velocity of 40 m/s and an Inlet Flow Angle of 60 degree



Scaled Residuals Jan 29, 2008
FLUENT 6.2 (2d, segregated, rngke)

Convergence was achieved after about 668 iterations with a residual value set to 0.00001.

Mass Imbalance ~ -0.0117 kg/s (about 4×10^{-5} % of the mass flow rate at inlet)

Total Gauge Pressure inlet based on the Mass Weighted Average ~ 3.0546 MPa

Total Gauge Pressure Outlet Based on the Mass Weighted Average ~ 1.3787 MPa

Figure 4.6 shows the convergence history of the solution after about 668 iterations for the case with inlet velocity of 40 m/s directed at 60 degree to the radial direction.

Convergence of residuals was achieved with residual monitoring criteria set to 0.00001.

The total gauge pressure at inlet was much higher than that at outlet which shows that the blade extracts some energy from the flow.

Figure 4.7 Contour Plot of Static Pressure Distribution at Inlet velocity of 40 m/s and an Inlet Flow Angle of 60 degree

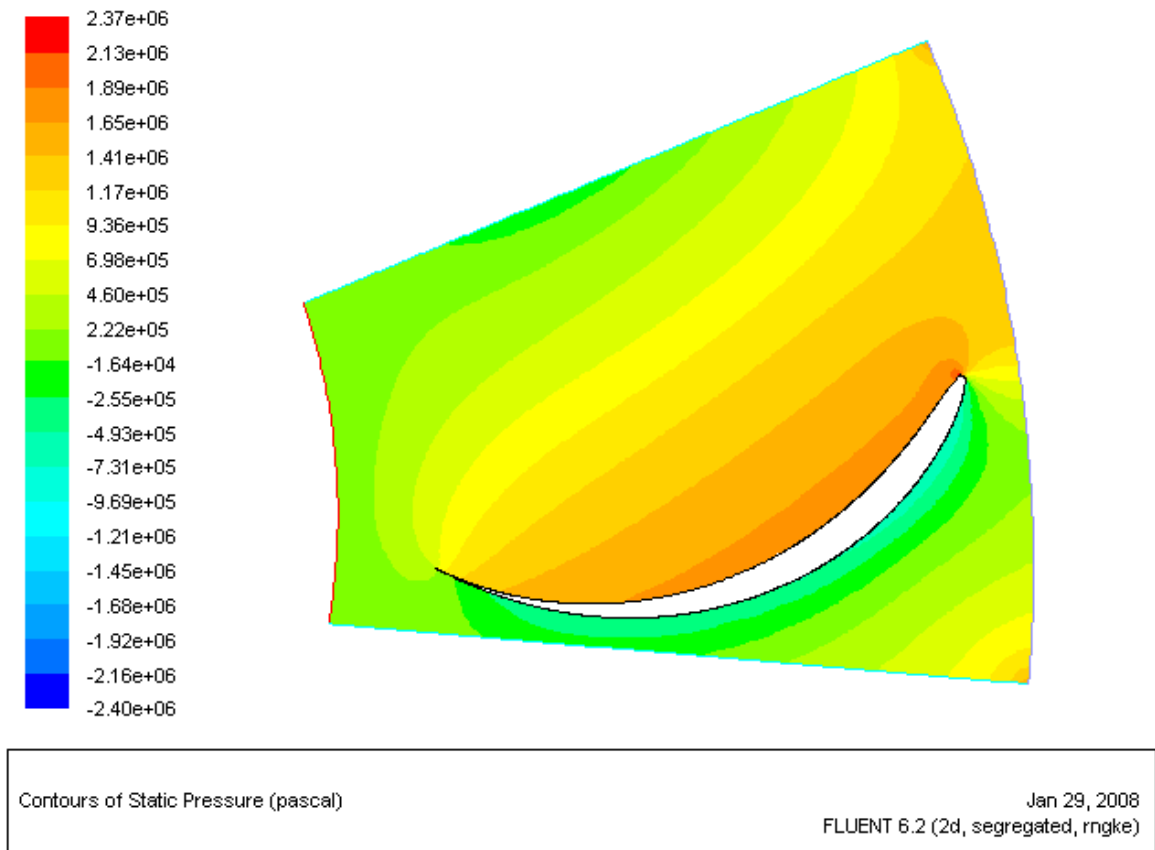
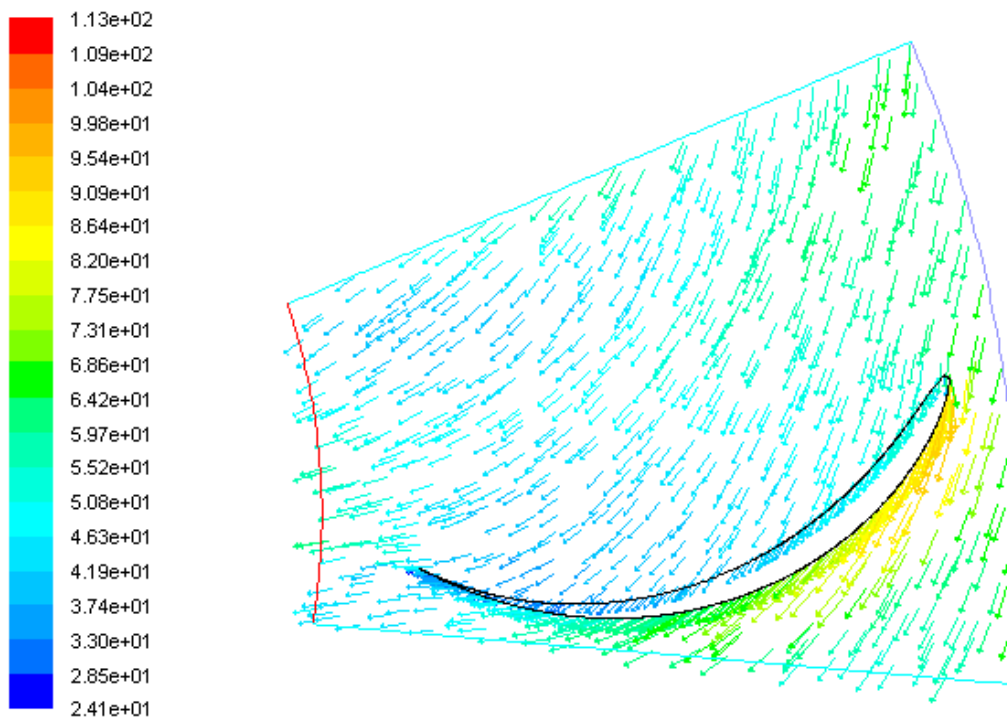


Figure 4.7 shows the static pressure contour plot for an inlet flow velocity of 40 m/s and directed at 60 degree to the radial direction. As with that static pressure contour plot

shown in Figure 4.2 cavitation was also present in this case. The plot also shows the reduction of pressure as fluid flow from the inlet to the exit. The pressure at the pressure side of the blade was higher than that at the suction side as expected. High pressures were observed at the stagnation points (inlet tip) of the blade. The drop in pressure observed at the back of the blade during the runner operation was also noticeable and that corresponds to where the negative pressures were observed.

Figure 4.8 Absolute Velocity Vector Plot at Inlet Velocity 40 m/s and an Inlet Flow Angle of 60 degree

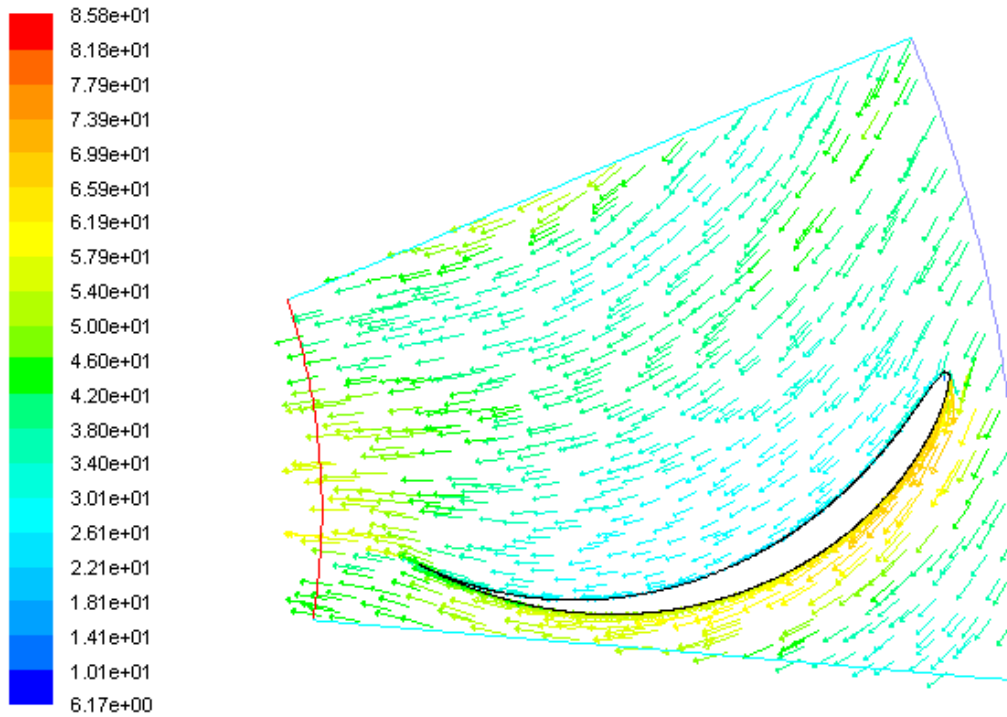


Velocity Vectors Colored By Velocity Magnitude (m/s)

Jan 29, 2008
FLUENT 6.2 (2d, segregated, rngke)

Figure 4.8 depicts the absolute velocity vector plot for an inlet flow velocity of 40 m/s and directed at 60 degree to the boundary at inlet. The velocities at the exit were lower as expected when compared to that at inlet. The velocities were higher at corresponding points on the suction side of the blade as compared to the pressure side with the flow hitting the pressure side of the blade.

Figure 4.9 Relative Velocity Vector Plot at Inlet Velocity of 40 m/s and an Inlet Flow Angle of 60 degree



relative-velocity Colored By Relative Velocity Magnitude (m/s) Jan 29, 2008
FLUENT 6.2 (2d, segregated, rngke)

Figure 4.9 shows the relative velocity vector plot for an inlet flow velocity of 40 m/s at 60 degree to the radial direction. The relative velocity was also higher at corresponding points on the suction side of the blade than the pressure side.

Figure 4.10 shows the discharge characteristic curve of the runner at a rotational speed of 115.4 rpm. Figures 4.11 to 4.13 show the corresponding hydraulic losses, net head, and power output characteristic curves of runner respectively. They were based on the neutralized values of these flow properties at a rotational speed of 115.4 rpm. Figure 4.14 shows the runner efficiency characteristic curve, also at a rotational speed of 115.4 rpm.

Figure 4.10 Plot of Inlet Flow Angle against Neutralized Discharge

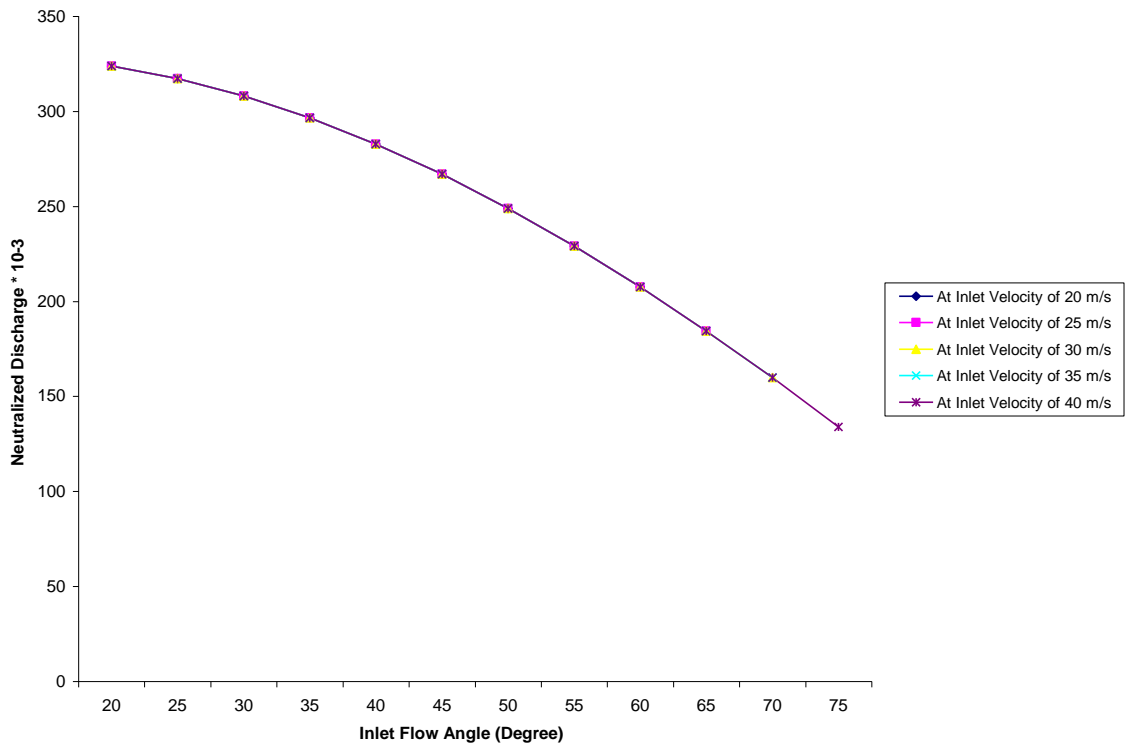


Figure 4.10 shows the plot of inlet flow angle against the neutralized discharge at different inlet velocities for the rotational speed of 115.4 rpm. The curves collapsed to form one single curve as expected; a function of the cosine of the flow angle. Thus at a constant velocity, the discharge is depended only on the flow direction and remains constant so long as the flow direction is constant. This also supports the negligible mass imbalance that came about during the CFD simulation.

Figure 4.11 Plot of Inlet Flow Angle against the Neutralized Hydraulic Losses

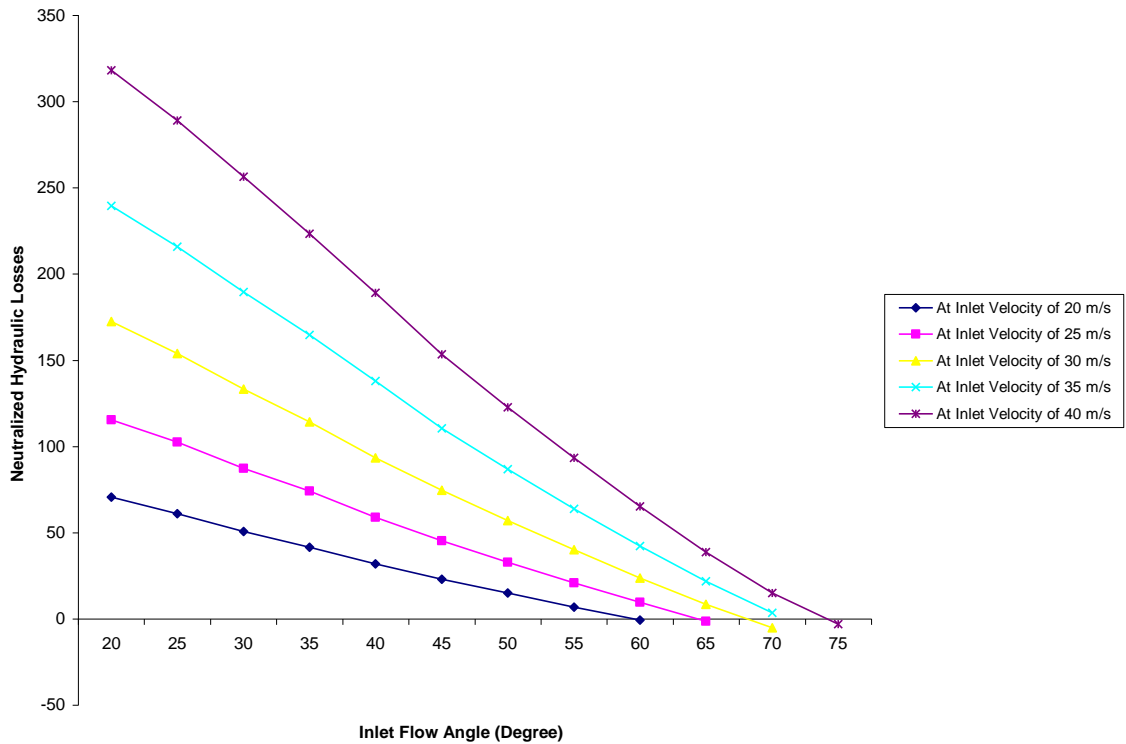


Figure 4.11 shows the plot of relative flow angle against the neutralized flow losses at five different inlet velocities for a rotational speed of 115.4 rpm. The hydraulic losses increase with increasing inlet velocity and decrease with decreasing discharge as controlled by the flow angle. The negative hydraulic losses observed in some cases were as a result of the effect of cavitation on the predictions of the pressure which was not factored in this study.

Figure 4.12 Plot of Inlet Flow Angle against the Neutralized Net Head

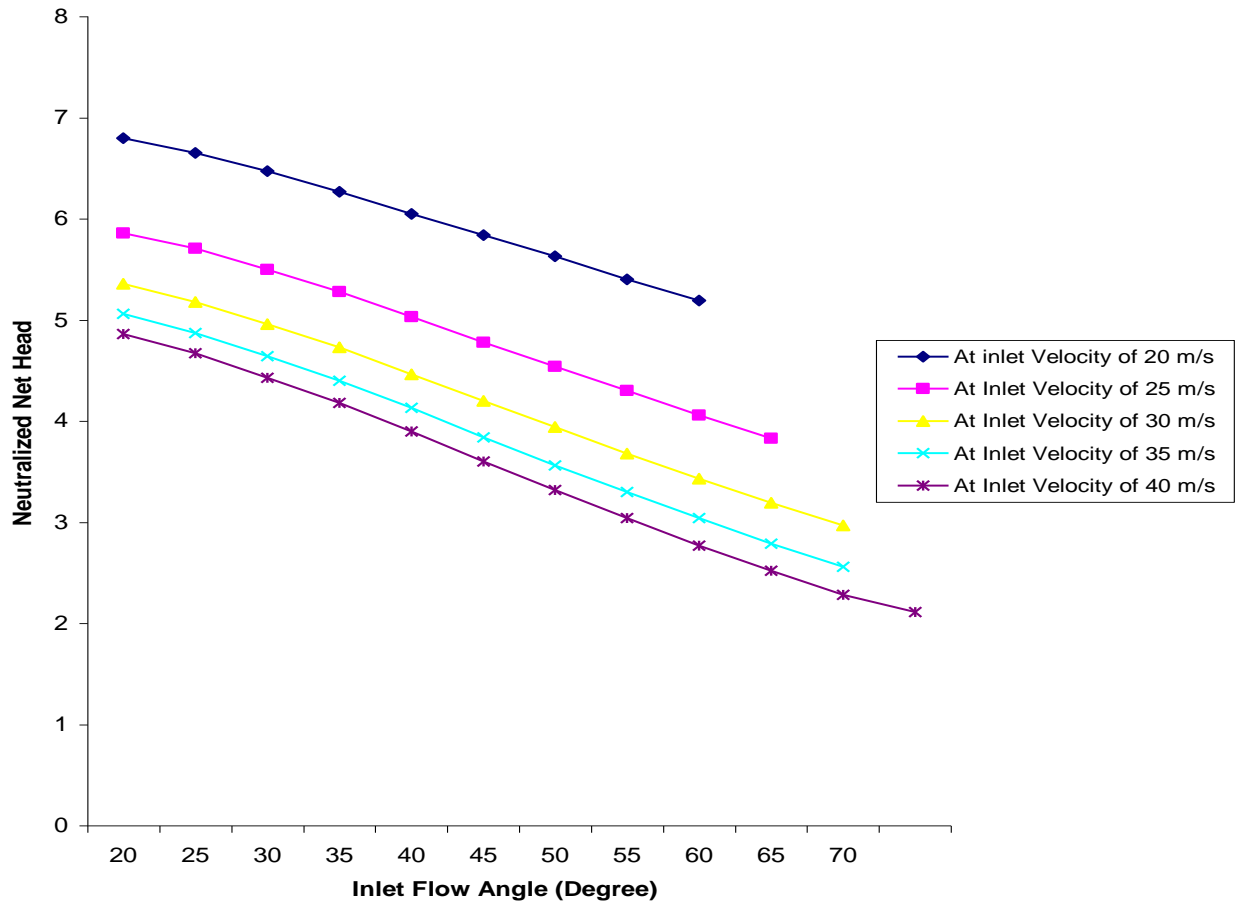


Figure 4.12 depicts plot of inlet flow angle against the neutralized net head for five different relative flow velocities at rotational speed of 115.4 rpm. The net head was comparatively higher for the case with lower inlet velocity and decreases with decreasing discharge. This might be due to the high hydraulic losses encountered with the higher inlet velocity flow.

Figure 4.13 Plot of Inlet Flow Angle against Neutralized Power Output

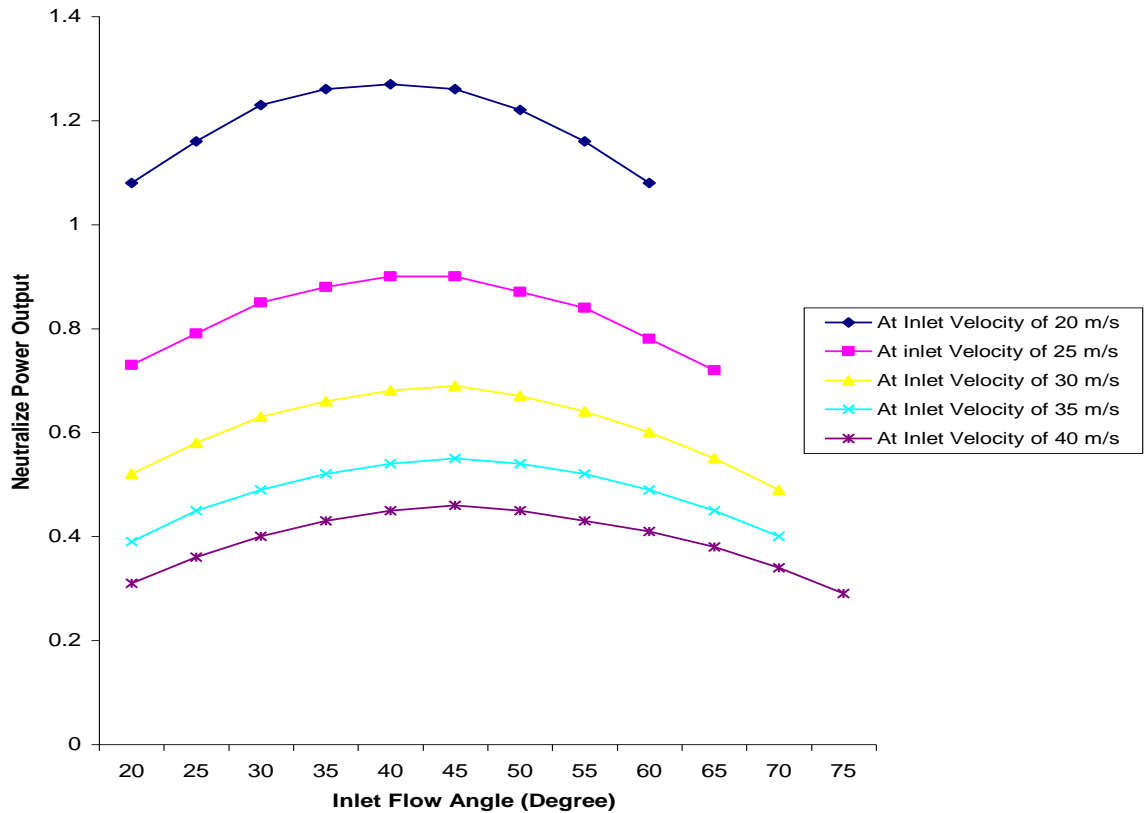
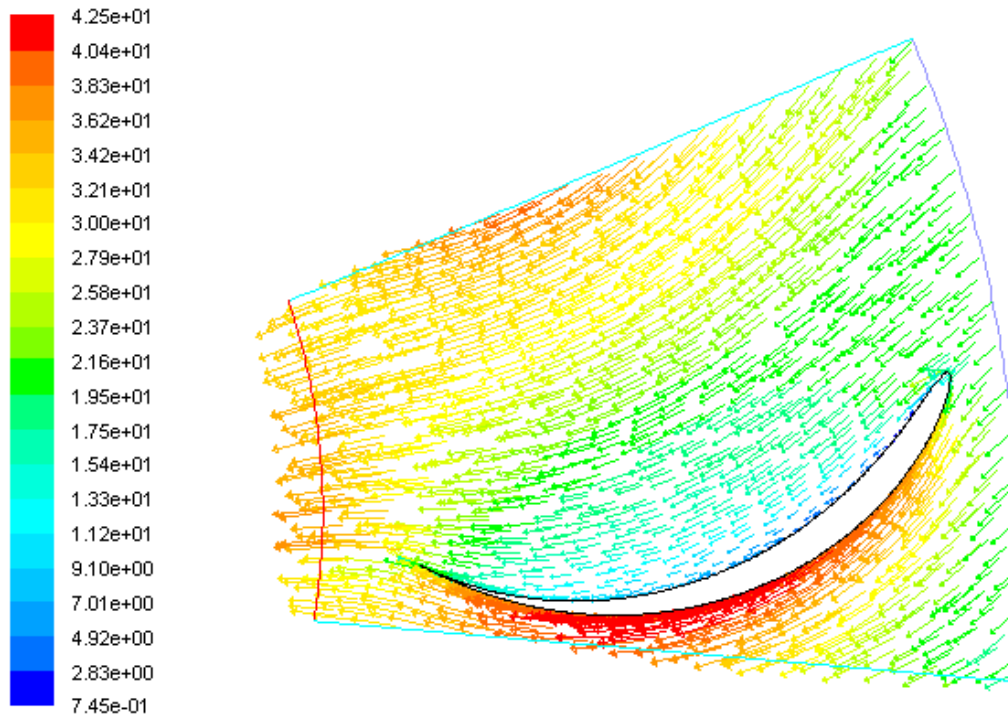


Figure 4.13 displays the plot of inlet flow angle against the neutralized power output for different inlet flow velocity at 115.4 rpm rotational speed. The power output rises steadily with increasing discharge to a point and decreases with further increase in discharge. The highest value was observed when the velocity inlet was 20 m/s, while the minimum occurred when the inlet velocity was 40 m/s, and this might be due to the increasing flow losses with increasing velocity. Figures 4.13.1 and 4.13.2 depict the relative velocity plot when the inlet velocity of 20 m/s and that with an inlet velocity of 40 m/s respectively each having a relative flow angle of 40 degree and at a rotational speed of 115.4 rpm. It would be observed that the losses were higher at inlet velocity of

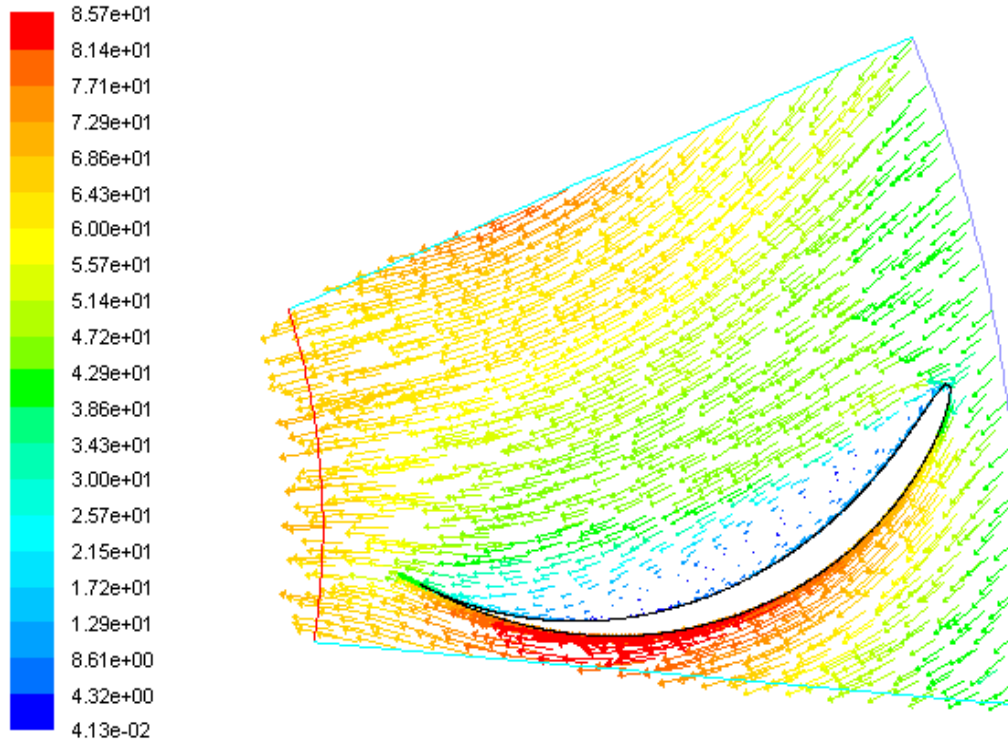
40 m/s (as shown by the flow recirculation and/or separation observed around the blade)
as compared to that with the inlet velocity of 20 m/s for the same flow angle.

Figure 4.13.1 Relative Velocity Vector plot of the Model at Inlet velocity of 20 m/s and
at Inlet Flow Angle of 40 degree.



relative-velocity Colored By Relative Velocity Magnitude (m/s) Nov 13, 2007
FLUENT 6.2 (2d, segregated, rngke)

Figure 4.13.2 Relative Velocity Vector plot of the Model at Inlet velocity of 40 m/s and at Inlet Flow Angle of 40 degree.



relative-velocity Colored By Relative Velocity Magnitude (m/s) Nov 13, 2007
FLUENT 6.2 (2d, segregated, rngke)

Figure 4.14 Plot of Inlet Flow Angle against Runner Efficiency

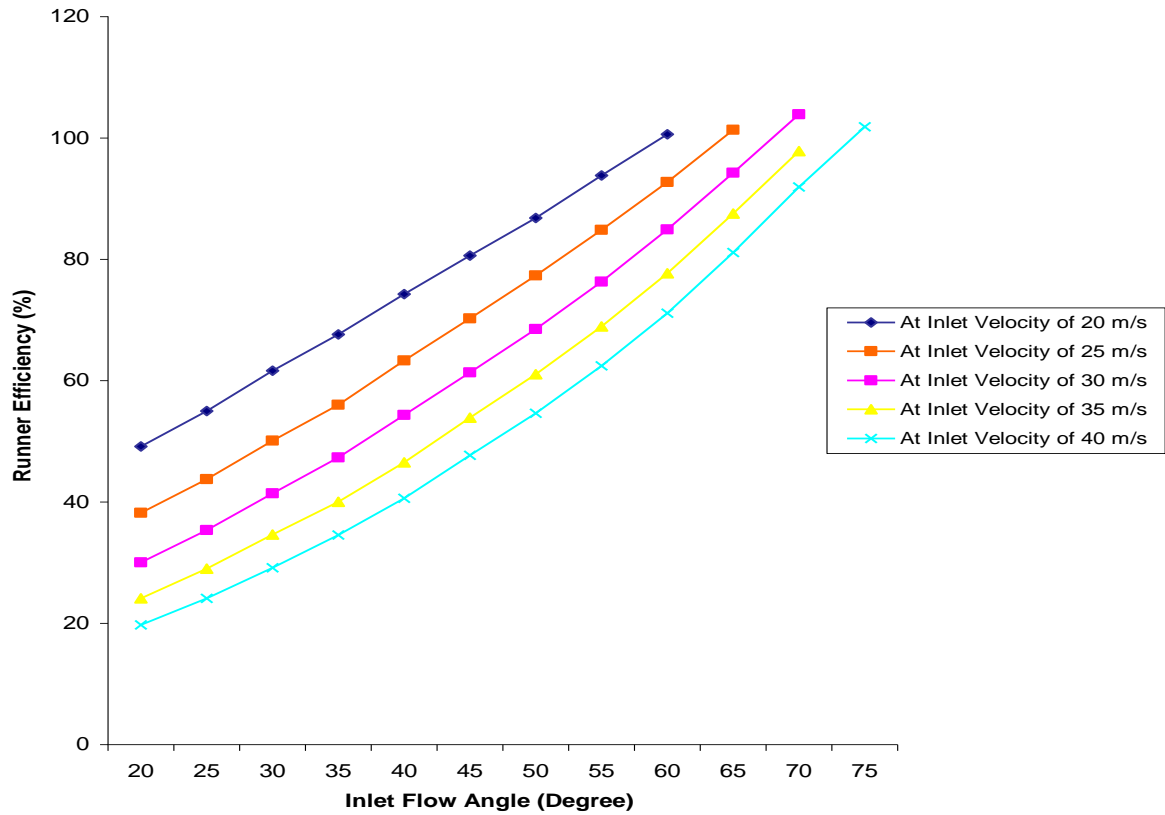


Figure 4.14 shows the plot of relative flow angle against the runner efficiency for different inlet flow velocity at 115.4 rpm rotational speed. The highest value was observed when the velocity inlet was 20 m/s, while the minimum occurred when the inlet velocity was 40 m/s, and this might be due to the increasing flow losses with increasing velocity as observed with the power output characteristic curves. The efficiency was slightly higher than 100 % in some cases and this might be because of the unaccounted effect of cavitation on the predictions. It would be observed that those points with such efficiency correspond to those conditions with negative hydraulic losses above in Figure 4.11 above.

Figures 4.15 to 4.19 display the respective discharge, net head, hydraulic losses, power output and runner efficiency at varying rotational velocity for an inlet flow velocity of 30 m/s.

Figure 4.15 Plot of Inlet Flow Angle against Neutralized Discharge at Varying Rotational Speed

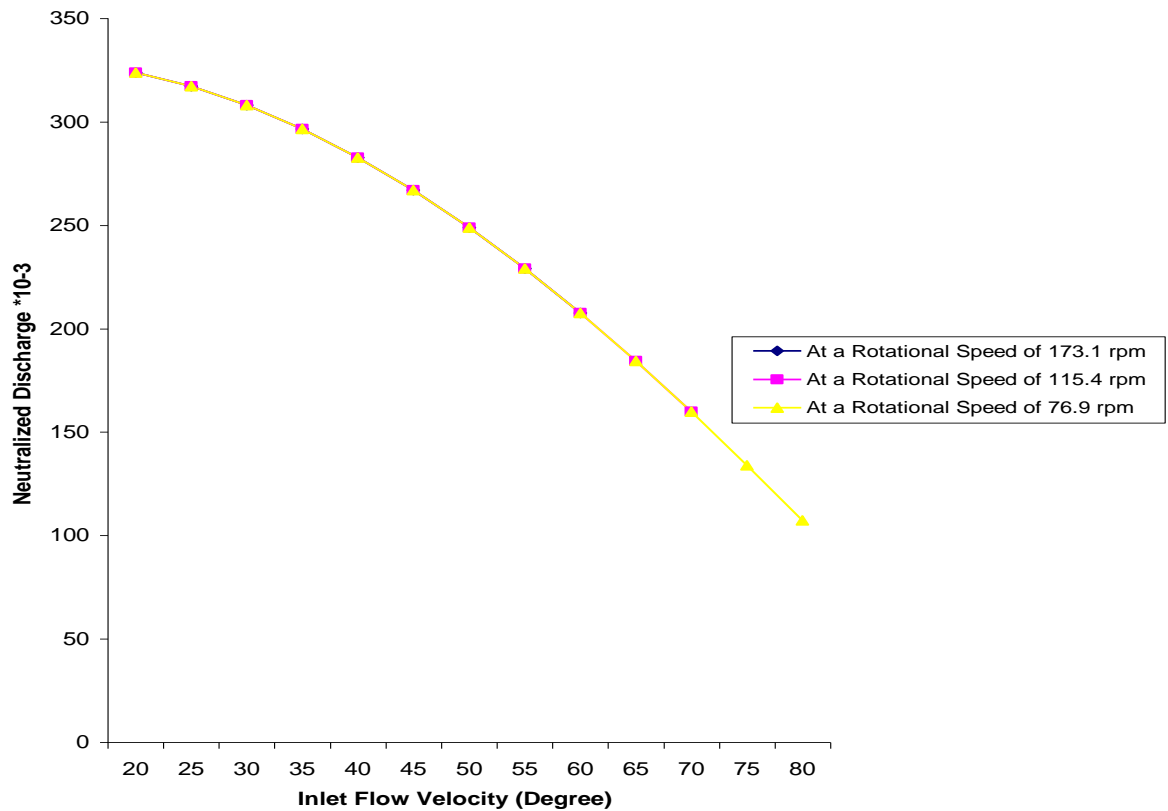


Figure 4.15 shows the discharge characteristic curve based on its neutralized value for an inlet velocity of 30 m/s at varying rotational speed of the runner. The discharges collapse to form one common curve. This is because the discharge is independent of the rotational speed at a constant flow velocity and flow direction.

Figure 4.16 Plot of Inlet Flow Angle against Neutralized Net Head at Varying Rotational Speed

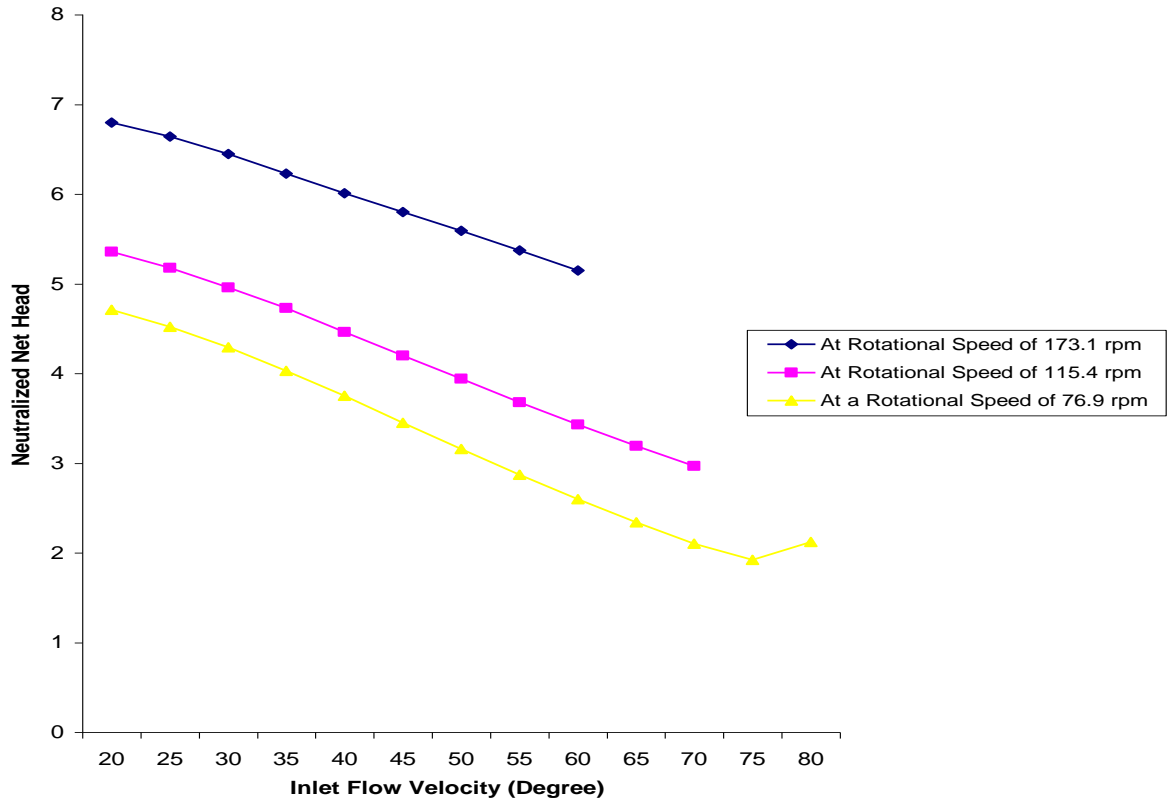


Figure 4.16 displays the net head characteristic curved based on its neutralized value for a flow inlet velocity of 30 m/s. The net head was higher when the rotational speed was increased. It was proportional to the rotational speed. The rise of net head at the flow angle of 80 degree might be as the result of the effect of cavitation which was not accounted for in the analysis.

Figure 4.17 Plot of Inlet Flow Angle against Neutralized Flow Losses at Varying Rotational Speed

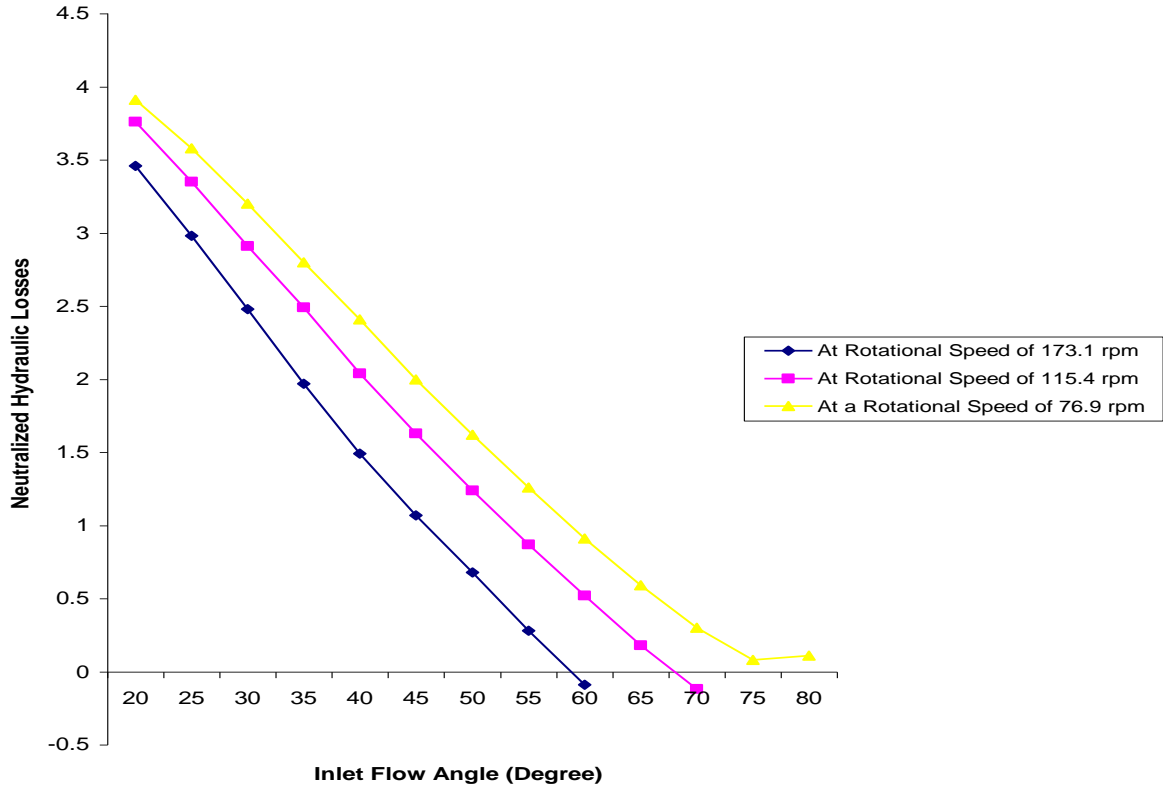


Figure 4.17 depicts the characteristic curve of the hydraulic flow losses based on its neutralized value for a flow inlet velocity of 30 m/s. The hydraulic losses as observed increased with decreasing rotational speed. The negative hydraulic losses observed in some of the flow angles might be as a result of cavitation which was unaccounted for in the analysis. Comparing Figure 4.17 to Figure 4.11, it would be observed that the inlet velocity has significant effect on the hydraulic losses than the rotational speed.

Figure 4.18 Plot of Inlet Flow Angle against Neutralized Power Output at Varying Rotational Speed

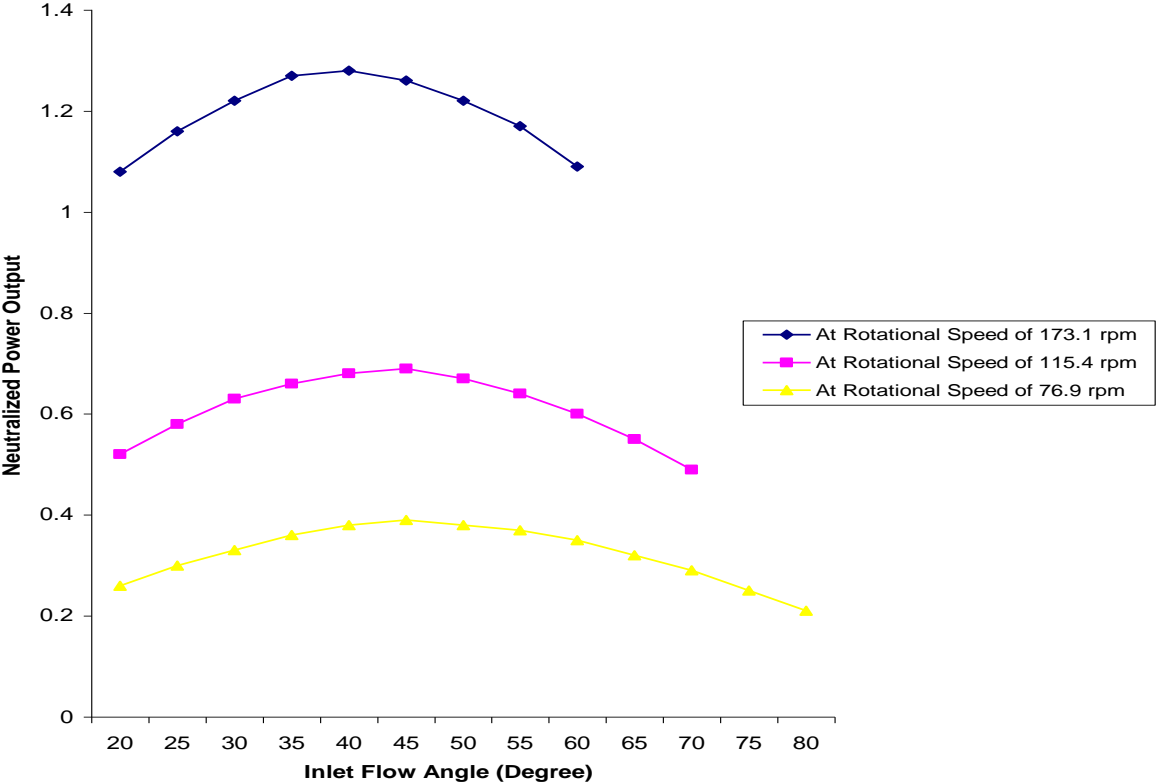
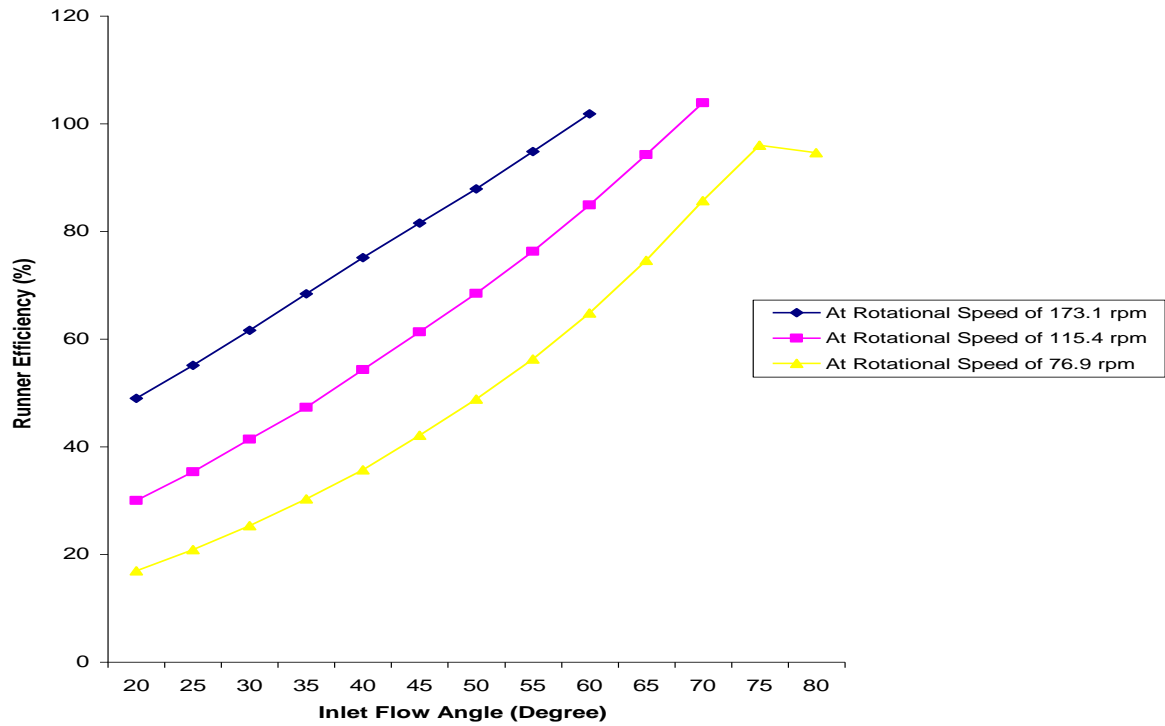


Figure 4.18 shows the characteristic curve of power output based on its neutralized value for the case with inlet flow velocity of 30 m/s. The power output was generally lower with the lowest rotational speed. It was proportional to the rotational speed.

Figure 4.19 Plot of Inlet Flow Angle against Runner Efficiency at Varying Rotational Speed



The Figure above (Figure 4.19) shows the runner efficiency characteristic curve at varying rotational speed for a flow inlet velocity of 30 m/s. The efficiency increased with increasing rotational speed and follows the same pattern. The sudden change of the curve from the relative flow angle of 75 degree for the case with the rotational speed of 76.9 rpm might be as a result of cavitation which was not accounted for. This effect was also witnessed in the hydraulic loss characteristic curve.

Table 1 depicts results of predictions obtained for the flow properties of interest at an inlet flow velocity of 20 m/s. The flow properties of concern were the discharge, torque, gross head, net head across the blade, and minimum pressure. From these quantities, the hydraulic losses, power output and their corresponding neutralized values for each of the range of angle subtended were also calculated. The properties were neutralized to enable them to be compared.

The discharge was calculated from the FLUENT flux report of the mass flow rate at inlet and outlet. The torque was calculated from the force and moment report on the blade about the center of rotation which is the origin in this case. The gross head represents the mass weighted average of total pressure head at inlet while the net head represents the mass weighted average of the difference in total pressure head at inlet and outlet.

The minimum pressure represents the minimum gauge static pressure in the flow domain. Tables 1 to 5 depict results of corresponding predictions for cases of flow inlet of 25, 30, 35 and 40 m/s, respectively. The rotational speed of the runner was at 173.1 rpm.

Tables 6-10 show results of predictions for the same cases and subtending the same angles aforementioned but with a rotational speed of 115.4 rpm; while Tables 11-15 shows the corresponding ones for a rotational speed of 76.9 rpm.

The gross head is the total pressure at the inlet to the model expressed as head while the net head is the difference in total pressure at inlet and outlet. The hydraulic losses flow energy loss as it passes through the rotor passage; they are calculated as the difference between the net head and the power output expressed as head (that is, dividing the power output with the product of the density, discharge and the free fall acceleration). The neutralized discharge is the discharge normalized with the product of the velocity and flow area while neutralized power output is the energy output normalized by the flow energy. The neutralized net head and neutralized hydraulic losses were the net head and hydraulic losses respectively normalized with their respective velocity head. The flow coefficient is the discharge divided by the product of the rotational speed and the cube of the diameter of the rotor. The head coefficient is the net head divided by the product of the square of both the rotational speed and the rotor diameter. The runner efficiency is the ratio of the power output to the flow power (based on the net head) expressed in percentage. The footnotes on each of the tables' further show how each of the flow properties were calculated.

CFD Predictions of Flow Properties

Rotational Speed of 173.1 rpm

Table 1 For the Case of Inlet velocity of 20 m/s

Inlet Flow Angle (deg.)	Discharge (m ³ /s)	Torque (MNm)	Gross Head ¹ (m)	Net Head ² (m)	Hydraulic Losses ³ (m)	Minimum Gauge Pressures (kPa)	Power Output (MW)	Neutralized Discharge ⁴ *10 ⁻³	Neutralized Power Output ⁵	Neutralized Net Head ⁶	Neutralized Hydraulic Losses ⁷	Flow Coefficient *10 ⁻³	Head Coefficient *10 ⁻³	Runner Efficiency (%)
20	22.7	1.77	280.4	203.8	59.9	-597.6	32.0	323.9	2.29	10.0	2.94	29.2	496.5	70.6
25	22.2	1.84	283.5	220.7	67.7	-505.8	33.3	317.2	2.38	10.8	3.32	28.6	537.6	69.3
30	21.6	1.89	284.7	218.4	56.1	-418.8	34.3	308.0	2.45	10.7	2.75	27.7	532.2	74.3
35	20.8	1.91	285.6	216.3	46.0	-333.7	34.7	296.5	2.48	10.6	2.26	26.7	527.0	78.7
40	19.8	1.90	286.3	214.1	36.8	-274.7	34.4	282.8	2.46	10.5	1.80	25.5	521.7	82.8
45	18.7	1.85	286.6	212.0	28.8	-208.4	33.6	266.9	2.40	10.4	1.41	24.0	516.6	86.4
50	17.4	1.78	286.2	208.8	19.6	-153.1	32.3	248.9	2.31	10.2	0.96	22.4	508.8	90.6
55	16.0	1.69	285.5	205.8	11.4	-171.2	30.6	229.1	2.18	10.1	0.56	20.6	501.4	94.4

¹ (ptotal[in])/ρg

² (ptotal[in] – ptotal[out])/ρg

³ {Net Head – (Power Output/ρgQ)}

⁴ Discharge/(A*Velocity) ; where A is Area per unit width rated in m² and was 3.5 m²

⁵ Power Output/(0.5 ρA *cubic Velocity); where ρ is density. 0.5ρA is rated in kg/m and was 1750 kg/m

⁶ Net Head/(square Velocity/2g); where g is the acceleration due to gravity = 9.81 m²/s

⁷ Hydraulic Losses/(square Velocity/2g); where g =9.81 m²/s

Table 1 reveals increasing efficiency up to an inlet angle of 55 degree. This yields a specific speed of 45.3, with the specific speed defined as $N_s = 1.167N P^{1/2}/H^{5/4}$ where N is in rpm, H in meters and P in Kilowatts. The maximum runner efficiency was 94.4%. The maximum power however was obtained at an angle of 35 degree, with a runner efficiency of 78.7%. The results look plausible except that the values of the minimum pressures are far too low because cavitation was not considered in the analysis. It is seen that as the relative flow inlet angle increases to 55 degree, the magnitude of the negative pressure decreases while the efficiency increases. Thus, at the near design conditions, (that is best runner efficiency), the cavitation problem is less severe for the off design conditions.

Table 2 For the Case of Inlet velocity of 25 m/s

Inlet Flow Angle (deg.)	Discharge (m ³ /s)	Torque (MNm)	Gross Head ⁸ (m)	Net Head ⁹ (m)	Hydraulic Losses ¹⁰ (m)	Minimum Gauge Pressures (kPa)	Power Output (MW)	Neutralized Discharge ¹¹ *10 ⁻³	Neutralized Power Output ¹²	Neutralized Net Head ¹³	Neutralized Hydraulic Losses ¹⁴	Flow Coefficient *10 ⁻³	Head Coefficient *10 ⁻³	Runner Efficiency
20	28.3	2.28	332.4	252.3	103.4	-1019.6	41.4	323.9	1.51	7.92	3.25	36.5	614.7	59.0
25	27.8	2.42	333.9	248.2	87.4	-892.0	43.8	317.2	1.60	7.79	2.74	35.7	604.7	64.8
30	27.0	2.52	333.7	242.7	70.3	-736.5	45.6	308.0	1.67	7.62	2.21	34.7	591.4	71.1
35	25.9	2.57	332.9	237.0	53.9	-613.5	46.6	296.5	1.70	7.44	1.69	33.4	577.3	77.3
40	24.7	2.58	331.0	230.9	38.5	-485.5	46.7	282.8	1.71	7.25	1.21	31.8	562.5	83.3
45	23.4	2.53	329.3	225.1	24.9	-397.1	45.9	266.9	1.68	7.07	0.78	30.0	548.5	88.9
50	21.8	2.44	327.1	218.9	11.6	-308.0	44.3	248.9	1.62	6.87	0.36	28.0	533.4	94.7
55	20.0	2.32	324.4	212.5	-1.5	-296.5	42.1	229.1	1.54	6.67	-0.05	25.8	517.6	100.7

⁸ (ptotal[in])/ρg

⁹ (ptotal[in] – ptotal[out])/ρg

¹⁰ {Net Head – (Power Output/ρgQ)}

¹¹ Discharge/(A*Velocity) ; where A is Area per unit width rated in m² and was 3.5 m²

¹² Power Output/(0.5 ρA *cubic Velocity); where ρ is density. 0.5ρA is rated in kg/m and was 1750 kg/m

¹³ Net Head/(square Velocity/2g); where g is the acceleration due to gravity = 9.81 m²/s

¹⁴ Hydraulic Losses/(square Velocity/2g); where g =9.81 m²/s

Table 2 reveals corresponding results for inlet velocity of 25 m/s. The maximum runner efficiency again occurs at an angle of 55 degree; however, its value is greater than 100% corresponding to negative hydraulic losses. The negative hydraulic losses rather add up (gives a positive impact) to the runner efficiency instead of decreasing it (giving it a negative impact); thus the runner efficiency that was calculated was excessive. This might be due to the effect of cavitation on the flow properties which were not accounted for in the single phase analysis as observed again with the unrealistic negative pressures which were inhibited in the predictions. The presence of vapor in the working fluid if considered in the solution is expected to increase the hydraulic losses making it positive in magnitude and thus reducing the runner efficiency what was predicted.

Table 3 For the Case of Inlet velocity of 30 m/s

Inlet Flow Angle (deg.)	Discharge (m ³ /s)	Torque (MNm)	Gross Head ¹⁵ (m)	Net Head ¹⁶ (m)	Hydraulic Losses ¹⁷ (m)	Minimum Pressures (kPa)	Power Output (MW)	Neutralized Discharge ¹⁸ *10 ⁻³	Neutralized Power Output ¹⁹	Neutralized Net Head ²⁰	Neutralized Hydraulic Losses ²¹	Flow Coefficient *10 ⁻³	Head Coefficient *10 ⁻³	Runner Efficiency
20	34.0	2.82	395.2	311.9	158.9	-1533.2	51.0	323.9	1.08	6.80	3.46	43.8	759.9	49.0
25	33.3	3.03	395.2	304.8	136.8	-1336.8	54.9	317.2	1.16	6.64	2.98	42.8	742.6	55.1
30	32.3	3.19	392.9	296.0	113.8	-1092.3	57.8	308.0	1.22	6.45	2.48	41.6	721.2	61.6
35	31.1	3.30	388.9	286.0	90.2	-908.3	59.8	296.5	1.27	6.23	1.97	40.1	696.7	68.4
40	29.7	3.33	383.9	275.9	68.6	-718.9	60.4	282.8	1.28	6.01	1.49	38.2	672.2	75.1
45	28.0	3.29	379.0	266.3	49.3	-595.7	59.7	266.9	1.26	5.80	1.07	36.0	648.7	81.5
50	26.1	3.19	373.8	256.6	31.2	-472.6	57.8	248.9	1.22	5.59	0.68	33.6	625.0	87.9
55	24.1	3.04	368.1	246.2	12.9	-436.1	55.1	229.1	1.17	5.37	0.28	30.9	599.9	94.8
60	21.8	2.84	362.4	236.2	-4.2	-377.2	51.4	207.5	1.09	5.15	-0.09	28.0	575.4	101.8

¹⁵ (ptotal[in])/ρg

¹⁶ (ptotal[in] – ptotal[out])/ρg

¹⁷ {Net Head – (Power Output/ρgQ)}

¹⁸ Discharge/(A*Velocity) ; where A is Area per unit width rated in m² and was 3.5 m²

¹⁹ Power Output/(0.5 ρA *cubic Velocity); where ρ is density. 0.5ρA is rated in kg/m and was 1750 kg/m

²⁰ Net Head/(square Velocity/2g); where g is the acceleration due to gravity = 9.81 m²/s

²¹ Hydraulic Losses/(square Velocity/2g); where g =9.81 m²/s

Table 3 shows the predictions for the corresponding inlet velocity of 30 m/s. It follows the same pattern of the previous ones described earlier. The maximum runner efficiency occurs at a slightly larger angle. The specific speed corresponding to the largest realistic runner efficiency (94.8%) was 48.6. The minimum pressure values are smaller than that for inlet velocity 25 m/s which is also smaller than that of 20 m/s.

Table 4 For the Case of Inlet velocity of 35 m/s

Inlet Flow Angle (deg.)	Discharge (m ³ /s)	Torque (MNm)	Gross Head ²² (m)	Net Head ²³ (m)	Hydraulic Losses ²⁴ (m)	Minimum Pressures (kPa)	Power Output (MW)	Neutralized Discharge ²⁵ *10 ⁻³	Neutralized Power Output ²⁶	Neutralized Net Head ²⁷	Neutralized Hydraulic Losses ²⁸	Flow Coefficient *10 ⁻³	Head Coefficient *10 ⁻³	Runner Efficiency
20	39.7	3.37	469.1	382.3	225.5	-2122.1	61.0	323.9	0.81	6.12	3.61	51.0	931.4	41.0
25	38.9	3.66	466.6	371.9	197.7	-1870.6	66.4	317.2	0.89	5.96	3.17	50.0	906.2	46.8
30	37.7	3.91	461.6	358.9	167.6	-1554.2	70.8	308.0	0.94	5.75	2.68	48.5	874.5	53.3
35	36.3	4.08	454.4	344.5	137.0	-1291.1	73.9	296.5	0.99	5.52	2.19	46.7	839.3	60.2
40	34.6	4.17	444.9	328.8	106.6	-1021.4	75.5	282.8	1.01	5.27	1.71	44.6	801.1	67.6
45	32.7	4.14	435.7	314.2	80.4	-828.0	75.0	266.9	1.00	5.03	1.29	42.1	765.4	74.4
50	30.5	4.02	426.4	299.6	56.0	-674.6	72.9	248.9	0.97	4.80	0.90	39.2	730.0	81.3
55	28.1	3.84	416.8	284.9	32.2	-605.9	69.6	229.1	0.93	4.56	0.52	36.1	694.2	88.7
60	25.4	3.59	407.4	270.5	9.5	-559.2	65.1	207.5	0.87	4.33	0.15	32.7	659.0	96.5

²² (ptotal[in])/ρg

²³ (ptotal[in] – ptotal[out])/ρg

²⁴ {Net Head – (Power Output/ρgQ)}

²⁵ Discharge/(A*Velocity) ; where A is Area per unit width rated in m² and was 3.5 m²

²⁶ Power Output/(0.5 ρA *cubic Velocity); where ρ is density. 0.5ρA is rated in kg/m and was 1750 kg/m

²⁷ Net Head/(square Velocity/2g); where g is the acceleration due to gravity = 9.81 m²/s

²⁸ Hydraulic Losses/(square Velocity/2g); where g =9.81 m²/s

Table 4 shows realistic efficiencies up to inlet flow angles of 60 degree. The minimum pressures were lower than the previous cases. The specific speed corresponding to the maximum efficiency was 47.0.

Table 5 For the Case of Inlet velocity of 40 m/s

Inlet Flow Angle (deg.)	Discharge (m ³ /s)	Torque (MNm)	Gross Head ²⁹ (m)	Net Head ³⁰ (m)	Hydraulic Losses ³¹ (m)	Minimum Pressures (kPa)	Power Output (MW)	Neutralized Discharge ³² *10 ⁻³	Neutralized Power Output ³³	Neutralized Net Head ³⁴	Neutralized Hydraulic Losses ³⁵	Flow Coefficient *10 ⁻³	Head Coefficient *10 ⁻³	Runner Efficiency
20	45.4	3.93	553.6	463.5	303.5	-2826.4	71.2	323.9	0.64	5.68	3.72	58.3	1129.2	34.5
25	44.4	4.33	548.5	449.2	268.9	-2470.9	78.6	317.2	0.70	5.51	3.30	57.1	1094.5	40.1
30	43.1	4.68	539.6	431.2	230.7	-2089.6	84.8	308.0	0.76	5.29	2.83	55.5	1050.5	46.5
35	41.5	4.91	528.8	412.2	193.5	-1738.1	89.0	296.5	0.80	5.05	2.37	53.4	1004.1	53.0
40	39.6	5.05	514.8	390.8	155.1	-1376.8	91.5	282.8	0.82	4.79	1.90	50.9	952.1	60.3
45	37.4	5.06	499.4	369.1	118.7	-1071.1	91.8	266.9	0.82	4.53	1.45	48.1	899.2	67.8
50	34.9	4.94	485.1	348.9	87.1	-884.1	89.5	248.9	0.80	4.28	1.07	44.8	850.1	75.0
55	32.1	4.72	470.6	328.7	56.6	-808.2	85.6	229.1	0.76	4.03	0.69	41.3	800.7	82.8
60	29.1	4.42	456.7	309.0	27.6	-733.0	80.2	207.5	0.72	3.79	0.34	37.4	752.9	91.1
65	25.8	4.05	443.7	290.0	-0.02	-567.1	73.4	184.4	0.66	3.56	0.00	33.2	706.5	100.0

²⁹ (ptotal[in])/ρg

³⁰ (ptotal[in] – ptotal[out])/ρg

³¹ {Net Head – (Power Output/ρgQ)}

³² Discharge/(A*Velocity) ; where A is Area per unit width rated in m² and was 3.5 m²

³³ Power Output/(0.5 ρA *cubic Velocity); where ρ is density. 0.5ρA is rated in kg/m and was 1750 kg/m

³⁴ Net Head/(square Velocity/2g); where g is the acceleration due to gravity = 9.81 m²/s

³⁵ Hydraulic Losses/(square Velocity/2g); where g =9.81 m²/s

Table 5 shows maximum runner efficiency at an angle of 65 degree and with lesser values of negative pressures. This runner efficiency might be excessive due to the negative hydraulic losses which follows the explanation made for the previous case (for table 2).

Comparison of the predictions from table 1 to 5 reveals a shift of maximum efficiency points with increasing inlet velocity. The optimum flow angle increases with increase in inlet velocity. The comparison also reveals an increase in the magnitude of the maximum negative pressure with increase in inlet velocity. The runner efficiencies observed for each of the cases might be higher than that expected due to the effect of cavitation which was not included in the analysis.

Rotational Speed of 115.4 rpm

Table 6 For the Case of Inlet velocity of 20 m/s

Inlet Flow Angle (deg.)	Discharge (m ³ /s)	Torque (MNm)	Gross Head ³⁶ (m)	Net Head ³⁷ (m)	Hydraulic Losses ³⁸ (m)	Minimum Pressures (kPa)	Power Output (MW)	Neutralized Discharge ³⁹ *10 ⁻³	Neutralized Power Output ⁴⁰	Neutralized Net Head ⁴¹	Neutralized Hydraulic Losses ⁴²	Flow Coefficient *10 ⁻³	Head Coefficient *10 ⁻³	Runner Efficiency
20	22.7	1.26	192.9	138.7	70.6	-650.4	15.2	323.9	1.08	6.80	3.46	43.8	761.2	49.1
25	22.2	1.35	176.2	135.7	61.0	-567.5	16.3	317.2	1.16	6.65	2.99	42.9	744.6	55.0
30	21.6	1.42	175.7	131.8	50.6	-469.1	17.2	308.0	1.23	6.47	2.48	41.6	723.5	61.6
35	20.8	1.46	173.7	127.8	41.4	-388.9	17.6	296.5	1.26	6.27	2.03	40.1	701.4	67.6
40	19.8	1.47	171.5	123.4	31.8	-306.7	17.8	282.8	1.27	6.05	1.56	38.2	677.0	74.2
45	18.7	1.46	169.3	119.0	23.0	-250.0	17.6	266.9	1.26	5.84	1.13	36.1	653.1	80.6
50	17.4	1.41	167.1	114.8	15.1	-194.4	17.0	248.9	1.22	5.63	0.74	33.6	630.0	86.8
55	16.0	1.35	164.5	110.1	6.8	-181.7	16.2	229.1	1.16	5.40	0.33	31.0	604.2	93.8
60	14.5	1.26	162.1	105.8	-0.7	-104.2	15.2	207.5	1.08	5.19	-0.03	28.0	580.4	100.6

³⁶ (ptotal[in])/ρg

³⁷ (ptotal[in] – ptotal[out])/ρg

³⁸ {Net Head – (Power Output/ρgQ)}

³⁹ Discharge/(A*Velocity) ; where A is Area per unit width rated in m² and was 3.5 m²

⁴⁰ Power Output/(0.5 ρA *cubic Velocity); where ρ is density. 0.5ρA is rated in kg/m and was 1750 kg/m

⁴¹ Net Head/(square Velocity/2g); where g is the acceleration due to gravity = 9.81 m²/s

⁴² Hydraulic Losses/(square Velocity/2g); where g =9.81 m²/s

Table 6 to 10 shows the predictions for rotational speed of 115.4 rpm at the same discharge and exit pressure as those of table 1 to 5; however, the gross head obtained from the calculation was different. This means the rotational speed has an upstream effect on the flow at the inlet of the runner.

Comparison of tables 6 to 10 against the corresponding tables 1 to 5 reveals that as the rotational runner speed decreases from 173.1 rpm to 115.4 rpm, the angle at which the maximum efficiency occurred increased. This is expected since maximum efficiency occurs when the relative flow is nearly tangential to blade inlet angle and therefore inlet flow angle must change with changing rotational speed to keep the relative flow pointing tangential to the blade inlet angle. The torque is also observed to decrease with decreasing rotational speed and since the power output is the product of the torque and the rotational speed, the power output drops rapidly.

Table 7 For the Case of Inlet velocity of 25 m/s

Inlet Flow Angle (deg.)	Discharge (m ³ /s)	Torque (MNm)	Gross Head ⁴³ (m)	Net Head ⁴⁴ (m)	Hydraulic Losses ⁴⁵ (m)	Minimum Pressures (kPa)	Power Output (MW)	Neutralized Discharge ⁴⁶ *10 ⁻³	Neutralized Power Output ⁴⁷	Neutralized Net Head ⁴⁸	Neutralized Hydraulic Losses ⁴⁹	Flow Coefficient *10 ⁻³	Head Coefficient *10 ⁻³	Runner Efficiency
20	28.3	1.64	227.2	186.7	115.4	-1055.0	19.8	323.9	0.73	5.86	3.62	54.7	1024.8	38.2
25	27.8	1.79	225.9	181.8	102.4	-913.7	21.6	317.2	0.79	5.71	3.21	53.6	997.5	43.7
30	27.0	1.92	223.2	175.1	87.3	-755.5	23.2	308.0	0.85	5.50	2.74	52.0	960.9	50.1
35	25.9	1.99	218.9	168.3	74.0	-636.9	24.0	296.5	0.88	5.28	2.32	50.1	923.8	56.0
40	24.7	2.04	213.8	160.2	58.8	-506.1	24.6	282.8	0.90	5.03	1.85	47.8	879.1	63.3
45	23.4	2.03	208.5	152.4	45.3	-397.1	24.5	266.9	0.90	4.78	1.42	45.1	836.2	70.2
50	21.8	1.98	203.3	144.7	32.9	-321.6	23.9	248.9	0.87	4.54	1.03	42.1	794.1	77.3
55	20.0	1.89	198.0	136.9	20.8	-252.6	22.8	229.1	0.84	4.30	0.65	38.7	751.5	84.8
60	18.2	1.77	192.9	129.5	9.5	-209.3	21.4	207.5	0.78	4.06	0.30	35.1	710.5	92.7
65	16.1	1.62	188.1	122.1	-1.5	-137.9	19.6	184.4	0.72	3.83	-0.05	31.1	670.1	101.3

⁴³ (ptotal[in])/ρg

⁴⁴ (ptotal[in] – ptotal[out])/ρg

⁴⁵ {Net Head – (Power Output/ρgQ)}

⁴⁶ Discharge/(A*Velocity) ; where A is Area per unit width rated in m² and was 3.5 m²

⁴⁷ Power Output/(0.5 ρA *cubic Velocity); where ρ is density. 0.5ρA is rated in kg/m and was 1750 kg/m

⁴⁸ Net Head/(square Velocity/2g); where g is the acceleration due to gravity = 9.81 m²/s

⁴⁹ Hydraulic Losses/(square Velocity/2g); where g =9.81 m²/s

Table 8 For the Case of Inlet velocity of 30 m/s

Inlet Flow Angle (deg.)	Discharge (m ³ /s)	Torque (MNm)	Gross Head ⁵⁰ (m)	Net Head ⁵¹ (m)	Hydraulic Losses ⁵² (m)	Minimum Pressures (kPa)	Power Output (MW)	Neutralized Discharge ⁵³ *10 ⁻³	Neutralized Power Output ⁵⁴	Neutralized Net Head ⁵⁵	Neutralized Hydraulic Losses ⁵⁶	Flow Coefficient *10 ⁻³	Head Coefficient *10 ⁻³	Runner Efficiency
20	34.0	2.04	289.2	246.0	172.3	-1534.9	24.6	323.9	0.52	5.36	3.76	65.7	1350.1	30.0
25	33.3	2.27	285.3	237.7	153.8	-1342.8	27.4	317.2	0.58	5.18	3.35	64.3	1304.5	35.3
30	32.3	2.48	279.7	227.6	133.3	-1103.8	29.9	308.0	0.63	4.96	2.91	62.4	1248.8	41.4
35	31.1	2.59	272.5	216.8	114.3	-899.3	31.3	296.5	0.66	4.73	2.49	60.1	1190.0	47.3
40	29.7	2.68	263.7	204.5	93.4	-715.6	32.4	282.8	0.68	4.46	2.04	57.3	1122.5	54.3
45	28.0	2.68	254.5	192.5	74.6	-558.7	32.4	266.9	0.69	4.20	1.63	54.1	1056.5	61.3
50	26.1	2.63	245.6	180.7	57.0	-454.9	31.7	248.9	0.67	3.94	1.24	50.5	991.8	68.5
55	24.1	2.52	236.7	168.9	40.0	-365.0	30.4	229.1	0.64	3.68	0.87	46.4	926.9	76.3
60	21.8	2.36	228.1	157.3	23.7	-308.2	28.6	207.5	0.60	3.43	0.52	42.1	863.4	84.9
65	19.4	2.17	220.1	146.3	8.4	-269.8	26.2	184.4	0.55	3.19	0.18	37.4	802.8	94.2
70	16.8	1.93	213.3	136.3	-5.3	-264.0	23.3	159.8	0.49	2.97	-0.12	32.4	748.2	103.9

⁵⁰ $(p_{total[in]})/\rho g$

⁵¹ $(p_{total[in]} - p_{total[out]})/\rho g$

⁵² $\{Net\ Head - (Power\ Output/\rho g Q)\}$

⁵³ $Discharge/(A * Velocity)$; where A is Area per unit width rated in m² and was 3.5 m²

⁵⁴ $Power\ Output/(0.5 \rho A * cubic\ Velocity)$; where ρ is density. $0.5\rho A$ is rated in kg/m and was 1750 kg/m

⁵⁵ $Net\ Head/(square\ Velocity/2g)$; where g is the acceleration due to gravity = 9.81 m²/s

⁵⁶ $Hydraulic\ Losses/(square\ Velocity/2g)$; where g = 9.81 m²/s

Table 9 For the Case of Inlet velocity of 35 m/s

Inlet Flow Angle (deg.)	Discharge (m ³ /s)	Torque (MNm)	Gross Head ⁵⁷ (m)	Net Head ⁵⁸ (m)	Hydraulic Losses ⁵⁹ (m)	Minimum Pressures (kPa)	Power Output (MW)	Neutralized Discharge ⁶⁰ *10 ⁻³	Neutralized Power Output ⁶¹	Neutralized Net Head ⁶²	Neutralized Hydraulic Losses ⁶³	Flow Coefficient *10 ⁻³	Head Coefficient *10 ⁻³	Runner Efficiency
20	39.7	2.45	361.8	315.7	239.6	-2121.1	29.6	323.9	0.39	5.06	3.84	76.6	1732.6	24.1
25	38.9	2.78	355.1	304.0	215.9	-1838.8	33.6	317.2	0.45	4.87	3.46	75.0	1668.1	29.0
30	37.7	3.07	345.8	289.5	189.5	-1528.1	37.0	308.0	0.49	4.64	3.03	72.9	1588.7	34.6
35	36.3	3.24	335.1	274.6	164.7	-1284.6	39.2	296.5	0.52	4.40	2.64	70.1	1507.1	40.0
40	34.6	3.37	322.4	257.8	138.0	-1015.8	40.7	282.8	0.54	4.13	2.21	66.9	1414.8	46.5
45	32.7	3.43	307.6	239.5	110.5	-754.4	41.4	266.9	0.55	3.84	1.77	63.1	1314.5	53.9
50	30.5	3.36	293.9	222.6	86.8	-617.3	40.6	248.9	0.54	3.56	1.39	58.9	1221.4	61.0
55	28.1	3.23	280.4	205.8	63.9	-503.0	39.0	229.1	0.52	3.30	1.02	54.2	1129.1	68.9
60	25.4	3.04	267.6	189.5	42.3	-402.3	36.7	207.5	0.49	3.04	0.68	49.1	1039.9	77.7
65	22.6	2.79	255.6	173.9	21.8	-414.0	33.7	184.4	0.45	2.79	0.35	43.6	954.5	87.5
70	19.6	2.49	245.4	159.9	3.4	-439.4	30.0	159.8	0.40	2.56	0.06	37.8	877.5	97.8

⁵⁷ (ptotal[in])/ρg

⁵⁸ (ptotal[in] – ptotal[out])/ρg

⁵⁹ {Net Head – (Power Output/ρgQ)}

⁶⁰ Discharge/(A*Velocity) ; where A is Area per unit width rated in m² and was 3.5 m²

⁶¹ Power Output/(0.5 ρA *cubic Velocity); where ρ is density. 0.5ρA is rated in kg/m and was 1750 kg/m

⁶² Net Head/(square Velocity/2g); where g is the acceleration due to gravity = 9.81 m²/s

⁶³ Hydraulic Losses/(square Velocity/2g); where g =9.81 m²/s

Table 10 For the Case of Inlet velocity of 40 m/s

Inlet Flow Angle (deg.)	Discharge (m ³ /s)	Torque (MNm)	Gross Head ⁶⁴ (m)	Net Head ⁶⁵ (m)	Hydraulic Losses ⁶⁶ (m)	Minimum Pressures (kPa)	Power Output (MW)	Neutralized Discharge ⁶⁷ *10 ⁻³	Neutralized Power Output ⁶⁸	Neutralized Net Head ⁶⁹	Neutralized Hydraulic Losses ⁷⁰	Flow Coefficient *10 ⁻³	Head Coefficient *10 ⁻³	Runner Efficiency
20	45.4	2.88	445.4	396.3	318.1	-2832.1	34.8	323.9	0.31	4.86	3.90	87.6	2174.7	19.7
25	44.4	3.30	434.9	380.5	288.9	-2437.4	39.9	317.2	0.36	4.67	3.54	85.7	2088.4	24.1
30	43.1	3.68	421.9	361.6	256.4	-2017.8	44.5	308.0	0.40	4.43	3.14	83.3	1984.4	29.1
35	41.5	3.96	406.4	340.9	223.4	-1684.9	47.9	296.5	0.43	4.18	2.74	80.2	1870.7	34.5
40	39.6	4.15	388.4	318.1	189.0	-1331.4	50.1	282.8	0.45	3.90	2.32	76.4	1745.6	40.6
45	37.4	4.25	367.6	293.4	153.3	-976.5	51.3	266.9	0.46	3.60	1.88	72.1	1610.1	47.7
50	34.9	4.18	348.3	270.5	122.7	-788.8	50.5	248.9	0.45	3.32	1.51	67.3	1484.6	54.6
55	32.1	4.03	329.4	247.9	93.3	-763.6	48.6	229.1	0.43	3.04	1.14	61.9	1360.3	62.4
60	29.1	3.79	311.4	226.0	65.2	-492.8	45.8	207.5	0.41	2.77	0.80	56.1	1240.0	71.1
65	25.8	3.49	294.7	205.1	38.7	-569.7	42.1	184.4	0.38	2.52	0.48	49.8	1125.7	81.1
70	22.4	3.11	280.4	186.3	15.1	-634.5	37.6	159.8	0.34	2.28	0.18	43.2	1022.6	91.9
75	18.8	2.66	270.9	171.8	-3.0	-686.2	32.2	134.0	0.29	2.11	-0.03	36.2	942.6	101.8

⁶⁴ $(p_{total[in]})/\rho g$

⁶⁵ $(p_{total[in]} - p_{total[out]})/\rho g$

⁶⁶ $\{Net\ Head - (Power\ Output/\rho g Q)\}$

⁶⁷ $Discharge/(A * Velocity)$; where A is Area per unit width rated in m² and was 3.5 m²

⁶⁸ $Power\ Output/(0.5 \rho A * cubic\ Velocity)$; where ρ is density. 0.5 ρA is rated in kg/m and was 1750 kg/m

⁶⁹ $Net\ Head/(square\ Velocity/2g)$; where g is the acceleration due to gravity = 9.81 m²/s

⁷⁰ $Hydraulic\ Losses/(square\ Velocity/2g)$; where g = 9.81 m²/s

Rotational Speed of 76.9 rpm

Table 11 For the Case of Inlet velocity of 20 m/s

Inlet Flow Angle (deg.)	Discharge (m ³ /s)	Torque (MNm)	Gross Head ⁷¹ (m)	Net Head ⁷² (m)	Hydraulic Losses ⁷³ (m)	Minimum Pressures (kPa)	Power Output (MW)	Neutralized Discharge ⁷⁴ *10 ⁻³	Neutralized Power Output ⁷⁵	Neutralized Net Head ⁷⁶	Neutralized Hydraulic Losses ⁷⁷	Flow Coefficient *10 ⁻³⁺	Head Coefficient *10 ⁻³	Runner Efficiency
20	22.7	0.92	128.9	109.1	76.0	-667.3	7.4	323.9	0.53	5.35	3.73	65.7	1348.8	30.4
25	22.2	1.01	127.4	105.8	68.5	-576.7	8.1	317.2	0.58	5.19	3.36	64.3	1307.9	35.3
30	21.6	1.10	125.0	101.3	59.3	-484.0	8.9	308.0	0.63	4.97	2.91	62.5	1251.7	41.4
35	20.8	1.14	121.7	96.9	51.6	-401.2	9.2	296.5	0.66	4.75	2.53	60.1	1197.2	46.7
40	19.8	1.18	117.8	91.5	42.5	-318.9	9.5	282.8	0.68	4.49	2.08	57.4	1130.4	53.5
45	18.7	1.19	113.7	86.0	33.7	-242.4	9.6	266.9	0.68	4.22	1.65	54.1	1062.4	60.8
50	17.4	1.16	109.7	80.7	25.9	-195.2	9.4	248.9	0.67	3.96	1.27	50.5	997.1	68.0
55	16.0	1.12	105.7	75.4	18.3	-154.9	9.0	229.1	0.64	3.70	0.90	46.5	932.2	75.7
60	14.5	1.05	101.9	70.4	11.2	-153.0	8.4	207.5	0.60	3.45	0.55	42.1	869.4	84.1
65	12.9	0.96	98.4	65.4	4.3	-79.5	7.7	184.4	0.55	3.21	0.21	37.4	808.6	93.5
70	11.2	0.86	95.3	60.9	-2.0	-90.1	6.9	159.8	0.49	2.99	-0.10	32.4	752.5	103.3

⁷¹ $(p_{total[in]})/\rho g$

⁷² $(p_{total[in]} - p_{total[out]})/\rho g$

⁷³ $\{Net\ Head - (Power\ Output/\rho g Q)\}$

⁷⁴ $Discharge/(A * Velocity)$; where A is Area per unit width rated in m² and was 3.5 m²

⁷⁵ $Power\ Output/(0.5 \rho A * cubic\ Velocity)$; where ρ is density. 0.5 ρA is rated in kg/m and was 1750 kg/m

⁷⁶ $Net\ Head/(square\ Velocity/2g)$; where g is the acceleration due to gravity = 9.81 m²/s

⁷⁷ $Hydraulic\ Losses/(square\ Velocity/2g)$; where g = 9.81 m²/s

Tables 11 to 15 present the predictions for the rotational speed of 76.9 rpm corresponding to those of tables 1 to 6 for rotational speed of 173.1 rpm and tables 7 to 10 for rotational speed of 115.4 rpm, respectively. The same trend observed when comparing the results of table 1 to 6 and table 7 to 10 is followed, confirming the previous discussion regarding effect of rotational speed.

Table 12 For the Case of Inlet velocity 25 m/s

Inlet Flow Angle (deg.)	Discharge (m ³ /s)	Torque (MNm)	Gross Head ⁷⁸ (m)	Net Head ⁷⁹ (m)	Hydraulic Losses ⁸⁰ (m)	Minimum Pressures (kPa)	Power Output (MW)	Neutralized Discharge ⁸¹ *10 ⁻³	Neutralized Power Output ⁸²	Neutralized Net Head ⁸³	Neutralized Hydraulic Losses ⁸⁴	Flow Coefficient *10 ⁻³	Head Coefficient *10 ⁻³	Runner Efficiency
20	28.3	1.21	179.3	157.3	122.4	-1046.9	9.7	323.9	0.36	4.94	3.84	82.1	1943.6	22.2
25	27.8	1.37	175.7	151.4	110.8	-914.9	11.0	317.2	0.40	4.75	3.48	80.4	1870.5	26.8
30	27.0	1.51	170.7	144.3	98.4	-761.5	12.1	308.0	0.44	4.53	3.09	78.1	1782.7	31.8
35	25.9	1.60	164.9	136.6	86.1	-637.6	12.9	296.5	0.47	4.29	2.70	75.2	1688.3	37.0
40	24.7	1.66	158.2	128.0	72.9	-502.8	13.4	282.8	0.49	4.02	2.29	71.7	1581.8	43.1
45	23.4	1.70	150.3	118.5	58.9	-373.1	13.7	266.9	0.50	3.72	1.85	67.7	1464.7	50.3
50	21.8	1.67	143.1	109.8	47.0	-297.8	13.4	248.9	0.49	3.45	1.47	63.1	1356.4	57.2
55	20.0	1.60	135.9	101.0	35.4	-261.4	12.9	229.1	0.47	3.17	1.11	58.1	1248.1	65.0
60	18.2	1.51	129.1	92.6	24.4	-229.7	12.1	207.5	0.44	2.91	0.77	52.6	1144.6	73.6
65	16.1	1.39	122.8	84.6	14.0	-164.9	11.2	184.4	0.41	2.66	0.44	46.7	1045.3	83.4
70	14.0	1.24	117.4	77.3	4.6	-197.5	10.0	159.8	0.36	2.43	0.14	40.5	955.1	94.1
75	11.7	1.06	113.9	71.8	-2.5	-45.1	8.5	134.0	0.31	2.25	-0.08	34.0	887.2	103.4

⁷⁸ (ptotal[in])/ρg

⁷⁹ (ptotal[in] – ptotal[out])/ρg

⁸⁰ {Net Head – (Power Output/ρgQ)}

⁸¹ Discharge/(A*Velocity) ; where A is Area per unit width rated in m² and was 3.5 m²

⁸² Power Output/(0.5 ρA *cubic Velocity); where ρ is density. 0.5ρA is rated in kg/m and was 1750 kg/m

⁸³ Net Head/(square Velocity/2g); where g is the acceleration due to gravity = 9.81 m²/s

⁸⁴ Hydraulic Losses/(square Velocity/2g); where g =9.81 m²/s

Table 13 For the Case of Inlet velocity of 30 m/s

Inlet Flow Angle (deg.)	Discharge (m ³ /s)	Torque (MNm)	Gross Head ⁸⁵ (m)	Net Head ⁸⁶ (m)	Hydraulic Losses ⁸⁷ (m)	Minimum Pressures (kPa)	Power Output (MW)	Neutralized Discharge ⁸⁸ *10 ⁻³	Neutralized Power Output ⁸⁹	Neutralized Net Head ⁹⁰	Neutralized Hydraulic Losses ⁹¹	Flow Coefficient *10 ⁻³	Head Coefficient *10 ⁻³	Runner Efficiency
20	34.0	1.51	240.5	216.0	179.5	-1520.4	12.2	323.9	0.26	4.71	3.91	98.6	2669.5	16.9
25	33.3	1.76	234.3	207.3	164.0	-1315.8	14.1	317.2	0.30	4.52	3.58	96.5	2561.2	20.9
30	32.3	1.96	226.3	196.6	146.8	-1080.4	15.8	308.0	0.33	4.29	3.20	93.7	2429.8	25.3
35	31.1	2.12	216.6	184.6	128.6	-890.7	17.1	296.5	0.36	4.03	2.80	90.2	2281.7	30.3
40	29.7	2.22	206.0	172.0	110.6	-704.7	17.9	282.8	0.38	3.75	2.41	86.0	2125.3	35.7
45	28.0	2.28	194.1	158.2	91.5	-526.9	18.3	266.9	0.39	3.45	2.00	81.2	1954.8	42.1
50	26.1	2.25	182.6	144.9	74.1	-407.1	18.1	248.9	0.38	3.16	1.62	75.7	1790.4	48.8
55	24.1	2.17	171.3	131.8	57.6	-339.7	17.5	229.1	0.37	2.87	1.26	69.7	1628.4	56.3
60	21.8	2.05	160.6	119.1	41.9	-183.3	16.5	207.5	0.35	2.60	0.91	63.1	1472.4	64.8
65	19.4	1.89	150.8	107.2	27.2	-263.1	15.2	184.4	0.32	2.34	0.59	56.1	1324.5	74.6
70	16.8	1.69	142.4	96.4	13.9	-326.7	13.6	159.8	0.29	2.10	0.30	48.6	1191.0	85.69
75	14.1	1.45	136.5	87.9	3.5	-125.7	11.6	134.0	0.25	1.92	0.08	40.8	1085.8	96.0
80	11.3	1.26	152.5	97.2	5.3	-256.0	10.2	107.2	0.21	2.12	0.11	32.6	1200.9	94.6

⁸⁵ (ptotal[in])/ρg

⁸⁶ (ptotal[in] – ptotal[out])/ρg

⁸⁷ {Net Head – (Power Output/ρgQ)}

⁸⁸ Discharge/(A*Velocity) ; where A is Area per unit width rated in m² and was 3.5 m²

⁸⁹ Power Output/(0.5 ρA *cubic Velocity); where ρ is density. 0.5ρA is rated in kg/m and was 1750 kg/m

⁹⁰ Net Head/(square Velocity/2g); where g is the acceleration due to gravity = 9.81 m²/s

⁹¹ Hydraulic Losses/(square Velocity/2g); where g =9.81 m²/s

Table 14 For the Case of Inlet velocity of 35 m/s

Inlet Flow Angle (deg.)	Discharge (m ³ /s)	Torque (MNm)	Gross Head ⁹² (m)	Net Head ⁹³ (m)	Hydraulic Losses ⁹⁴ (m)	Minimum Pressures (kPa)	Power Output (MW)	Neutralized Discharge ⁹⁵ *10 ⁻³	Neutralized Power Output ⁹⁶	Neutralized Net Head ⁹⁷	Neutralized Hydraulic Losses ⁹⁸	Flow Coefficient *10 ⁻³	Head Coefficient *10 ⁻³	Runner Efficiency
20	39.7	1.84	312.4	285.5	247.5	-2103.0	14.8	323.9	0.20	4.57	3.96	115.0	3528.0	13.3
25	38.9	2.18	302.8	272.8	226.8	-1811.7	17.5	317.2	0.23	4.37	3.63	112.6	3371.5	16.9
30	37.7	2.47	291.2	258.2	204.6	-1498.1	19.9	308.0	0.26	4.14	3.28	109.3	3191.4	20.8
35	36.3	2.69	277.6	241.9	181.2	-1244.2	21.7	296.5	0.29	3.88	2.90	105.2	2989.9	25.1
40	34.6	2.85	262.2	224.0	156.6	-980.7	22.9	282.8	0.31	3.59	2.52	100.4	2768.7	30.1
45	32.7	2.95	244.7	204.6	130.7	-703.9	23.7	266.9	0.32	3.28	2.09	94.7	2528.5	36.1
50	30.5	2.92	228.0	185.9	107.2	-548.5	23.5	248.9	0.31	2.98	1.72	88.4	2297.4	42.3
55	28.1	2.83	211.8	167.6	85.0	-457.6	22.8	229.1	0.30	2.68	1.36	81.3	2071.3	49.3
60	25.4	2.67	196.5	150.0	63.8	-383.8	21.5	207.5	0.29	2.40	1.02	73.7	1853.4	57.5
65	22.6	2.46	182.4	133.3	43.9	-373.2	19.8	184.4	0.26	2.13	0.70	65.4	1647.3	67.1
70	19.6	2.20	170.2	118.3	26.0	-180.4	17.7	159.8	0.24	1.89	0.42	56.7	1461.5	78.1
75	16.4	1.89	161.4	106.1	11.6	-220.2	15.2	134.0	0.20	1.70	0.19	47.6	1311.1	89.1
80	13.1	1.65	183.5	120.4	17.1	-355.7	13.3	107.2	0.18	1.93	0.27	38.1	1487.6	85.8

⁹² (ptotal[in])/ρg

⁹³ (ptotal[in] – ptotal[out])/ρg

⁹⁴ {Net Head – (Power Output/ρgQ)}

⁹⁵ Discharge/(A*Velocity) ; where A is Area per unit width rated in m² and was 3.5 m²

⁹⁶ Power Output/(0.5 ρA *cubic Velocity); where ρ is density. 0.5ρA is rated in kg/m and was 1750 kg/m

⁹⁷ Net Head/(square Velocity/2g); where g is the acceleration due to gravity = 9.81 m²/s

⁹⁸ Hydraulic Losses/(square Velocity/2g); where g =9.81 m²/s

Table 15 For the Case of Inlet velocity of 40 m/s

Inlet Flow Angle (deg.)	Discharge (m ³ /s)	Torque (MNm)	Gross Head ⁹⁹ (m)	Net Head ¹⁰⁰ (m)	Hydraulic Losses ¹⁰¹ (m)	Minimum Pressures (kPa)	Power Output (MW)	Neutralized Discharge ¹⁰² *10 ⁻³	Neutralized Power Output ¹⁰³	Neutralized Net Head ¹⁰⁴	Neutralized Hydraulic Losses ¹⁰⁵	Flow Coefficient *10 ⁻³	Head Coefficient *10 ⁻³	Runner Efficiency
20	45.4	2.17	395.1	365.6	326.3	-2748.9	17.5	323.9	0.16	4.48	4.00	131.4	4517.4	10.7
25	44.4	2.61	381.7	348.9	300.6	-2371.4	21.0	317.2	0.19	4.28	3.69	128.7	4311.5	13.8
30	43.1	3.02	365.2	328.9	271.3	-1984.4	24.3	308.0	0.22	4.03	3.33	124.9	4064.2	17.5
35	41.5	3.32	346.8	307.5	241.8	-1634.6	26.75	296.5	0.24	3.77	2.971	120.3	3799.6	21.3
40	39.6	3.55	326.0	283.7	210.2	-1.282.5	28.5	282.8	0.25	3.48	2.58	114.7	3506.3	25.9
45	37.4	3.68	303.0	258.4	177.6	-931.8	29.61	266.9	0.26	3.17	2.18	108.2	3193.1	31.38
50	34.9	3.68	279.5	233.0	146.3	-699.9	29.6	248.9	0.26	2.86	1.79	101.0	2879.4	37.2
55	32.1	3.56	257.5	208.6	117.4	-586.4	28.7	229.1	0.26	2.56	1.44	92.9	2577.8	43.7
60	29.1	3.37	236.7	185.1	89.9	-457.6	27.1	207.5	0.24	2.27	1.10	84.2	2287.7	51.4
65	25.8	3.11	217.5	163.0	64.1	-495.4	25.0	184.4	0.22	2.00	0.79	74.8	2013.9	60.7
70	22.4	2.78	201.0	143.0	40.8	-269.5	22.4	159.8	0.20	1.75	0.50	64.8	1766.8	71.4
75	18.8	2.39	188.7	126.6	21.9	-328.8	19.3	134.0	0.17	1.55	0.27	54.4	1564.1	82.7
80	15.0	2.09	217.6	145.8	31.3	-462.7	16.9	107.2	0.15	1.79	0.38	43.5	1802.2	78.5

The minimum pressures for all the cases were negative and this indicate cavitation.

⁹⁹ (ptotal[in])/ρg

¹⁰⁰ (ptotal[in] – ptotal[out])/ρg

¹⁰¹ {Net Head – (Power Output/ρgQ)}

¹⁰² Discharge/(A*Velocity) ; where A is Area per unit width rated in m² and was 3.5 m²

¹⁰³ Power Output/(0.5 ρA *cubic Velocity); where ρ is density. 0.5ρA is rated in kg/m and was 1750 kg/m

¹⁰⁴ Net Head/(square Velocity/2g); where g is the acceleration due to gravity = 9.81 m²/s

¹⁰⁵ Hydraulic Losses/(square Velocity/2g); where g=9.81 m²/s

On a whole, it would be observed that the flow pattern was the same throughout all the cases. Cavitation occurred in all the cases under study. This resulted in the observation of non-physical negative pressures. The single phase solution did not incorporate the mass transfer from the liquid phase to the vapor phase and thus the need of a multiphase analysis to incorporate this transfer of mass into the solution. The next chapter depicts results with incorporates the effect of cavitation for the case with relative flow angle of 60 degree at an inlet velocity of 40 m/s.

CHAPTER FIVE

CAVITATION MODELING AND ANALYSIS

5.0 Introduction

Flow through hydraulic turbines is characterized with areas of low pressures. When the pressure in such areas fall below the saturated vapor pressure, intensive transition from the nuclear boundary of the liquid into a gaseous state is observed, which lead to discontinuities (cavities) filled with vapor. The formation of these discontinuities in a turbulence liquid flow is called cavitation [Krivchenko, 1986]²².

The existence of such cavities consist of two phases: formation and growth, the period of time during which the flow passes the region where the pressure drops, and collapses when it gets to a region where the pressure increases [Krivchenko, 1986]²². This phenomenon creates a mixture of liquid water and gaseous vapor within the flowing domain. A multiphase analysis is therefore required to model such phenomenon to accommodate the mass transfer from liquid to vapor and back to liquid. This section describes such an analysis and compares its results to that of a single phase analysis discussed in the previous chapter.

5.1 Modeling Cavitation

The modeling of cavitation follows similar modeling techniques described for the single phase; however, another (secondary) phase and its interaction to the already present primary phase (water) is incorporated into the flowing domain making the working fluid

a mixture of two phases. This was achieved by activating the multiphase model and defining the mixture (phases) and their interaction that exist between them (cavitation in this case). The under-relaxation factor for the cavitation modeling, unlike that for the single phase modeling was reduced to enable the solution to converge.

5.2 Results and Comparative Analysis

This section presents results obtained for the cavitation analysis of the periodic blade to blade flow discussed in chapter five. This is for the case with the flow at an inlet velocity of 40 m/s directed at an inlet flow angle of 60 degree with the runner rotating at 115.4 rpm. The results were compared to that of the single phase analysis shown in Figures 4.7 to 4.9. Only a single case was predicted since it suffices to show cavitation effect on modeling. Also it was found that it was much more difficult to get well converged solutions with the two-phase cavitation model and the solution requires much more computational time.

Figure 5.1 shows the convergence history of the solution after about 3750 iterations. It is clear that the mass residual have drops by five orders of magnitude and that all other residuals have dropped also, indication good convergence.

Figure 5.2 depicts the static pressure distribution of the mixture within the model while Figures 5.3 and 5.4 show respectively the absolute and the relative velocity vector plot of the mixture (liquid water and water vapor).

Figure 5.5 displays the volume fraction of the liquid water with respect to the vapor in the mixture since there are only two phases; while Figure 5.6 shows the volume fraction of vapor with respect to the liquid water in the mixture. They reveal the fraction of each of the phases in the mixtures at various points in the flowing domain.

Figure 5.1 Convergence History of the Solution for the case with Inlet Flow angle of 60 degree at 40 m/s inlet velocity

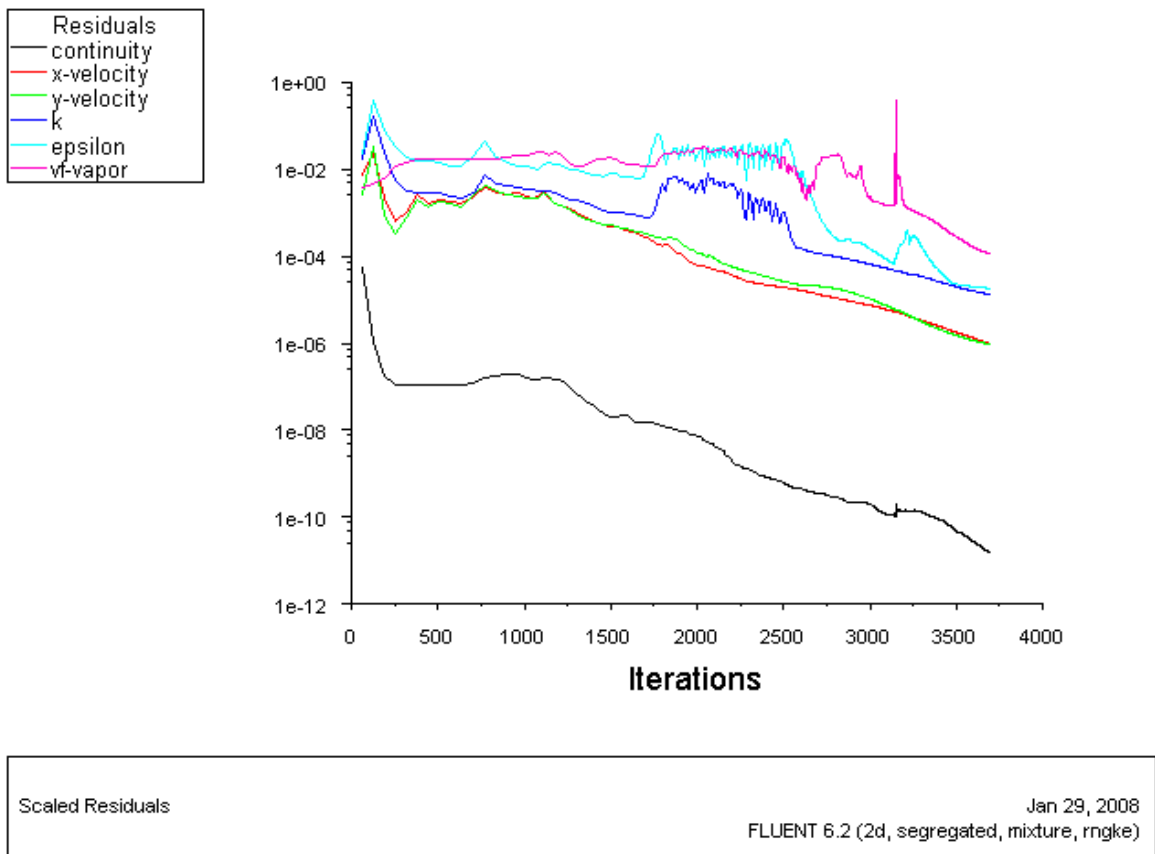
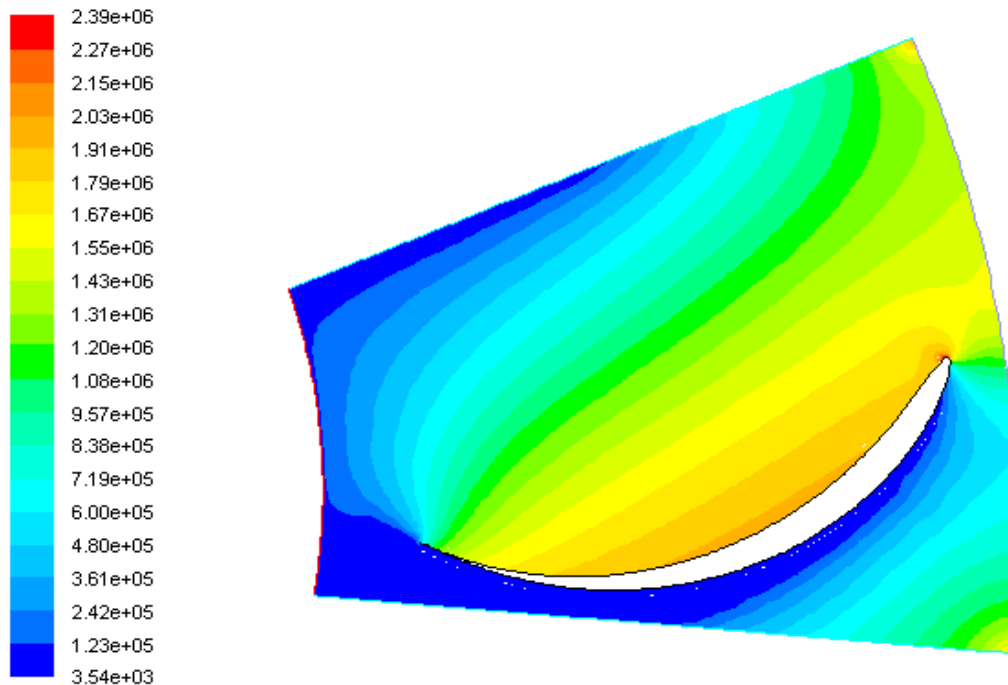


Figure 5.1 shows the convergence history of the solution. The solution converged after about 3750 iterations with a residual value set to 0.001. The mass imbalance observed was approximately -0.0488 kg/s (about $1.7 \times 10^{-4}\%$ of the mass flow rate at inlet).

The mass residual have dropped significantly and all other residuals have also dropped, and this indicates good convergence. There was some instability in the solution, however, they settle as the solution approached convergence. The total pressure at inlet based on the mass weighted average was 2.8087 MPa and that of the outlet was 1.7138 MPa indicating that the blade extracts some energy in the flowing fluid.

Figure 5.2 Static Absolute Pressure Contour Plot for the case with Inlet Flow angle of 60 degree at 40 m/s inlet velocity



Contours of Static Pressure (mixture) (pascal) Jan 29, 2008
FLUENT 6.2 (2d, segregated, mixture, rngke)

Figure 5.2 shows the static pressure distribution of the mixture. It is noticed that all pressure values are realistic and that there are no negative pressures. The corresponding figure for the single phase analysis, Figure 4.7 had revealed unrealistically low negative gauge pressures. In comparison between Figure 5.2 and Figure 4.7, it is important to note that the former presents absolute pressures whereas the latter presents gauge pressures. The lowest pressures were found at the suction side of the blade. These are the areas where cavitation occurs. The highest pressure was observed at the stagnation point and it is virtually the same in magnitude for both the single and multiphase analysis. This observation is in conformity with what was obtained in the “Cavitation Modeling of Water Pump” a tutorial handout in FLUENT tutorial documentary [FLUENT Documentary, 2004-2005]¹⁵.

Figure 5.3 Absolute Velocity Vector Plot for the case with Inlet Flow angle of 60 degree
at 40 m/s inlet velocity

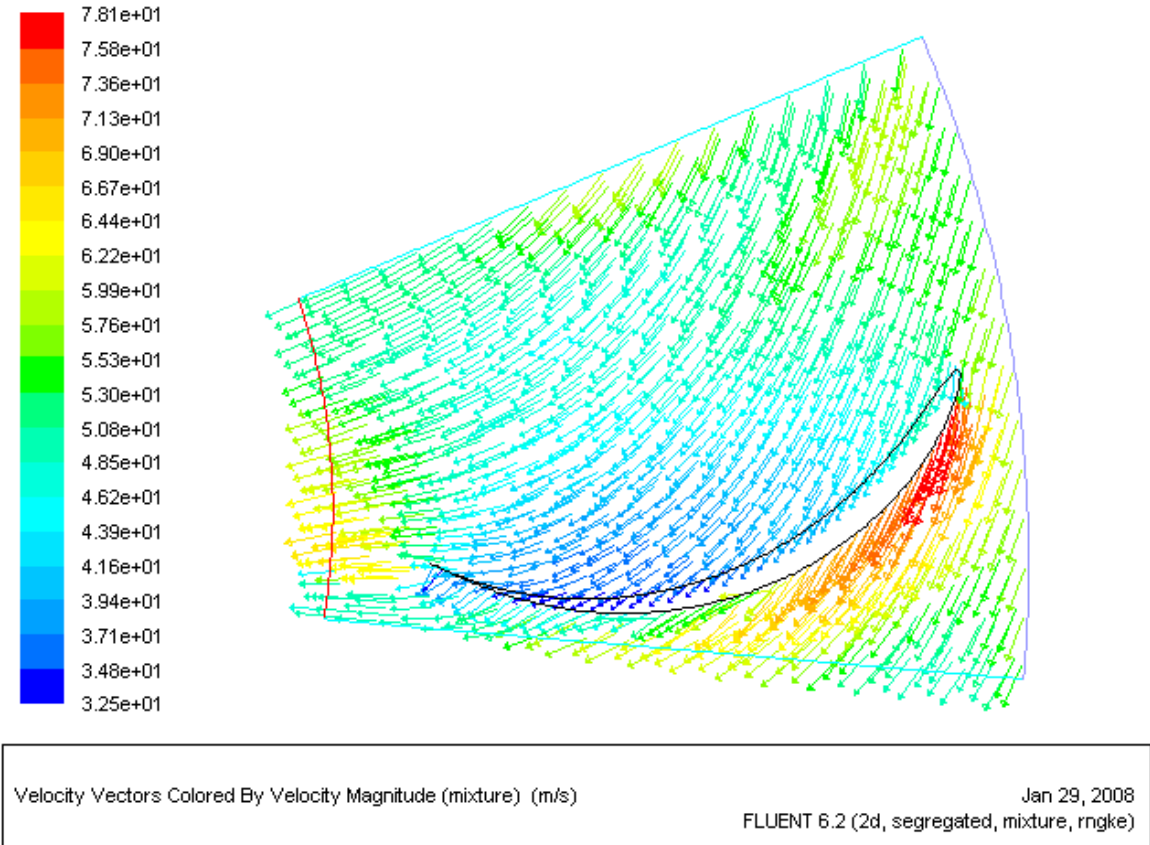


Figure 5.3 shows the absolute velocity distribution along the blade. The flow hits the suction side with approximately the same angles and magnitudes observed with the single phase. The high velocity observed just as the flow leaves the stagnation point to the suction point was lower in magnitude when compared with that for the single phase analysis shown in Figure 4.8. At the areas where the lowest velocities are observed, those velocities were higher in magnitude than that obtained for the single phase analysis. However, there is no significant difference in the velocity distribution pattern along the blade for both the single and the multiple phase analysis.

Figure 5.4 Relative Velocity Vector Plot for the case with Inlet Flow angle of 60 degree
at 40 m/s inlet velocity

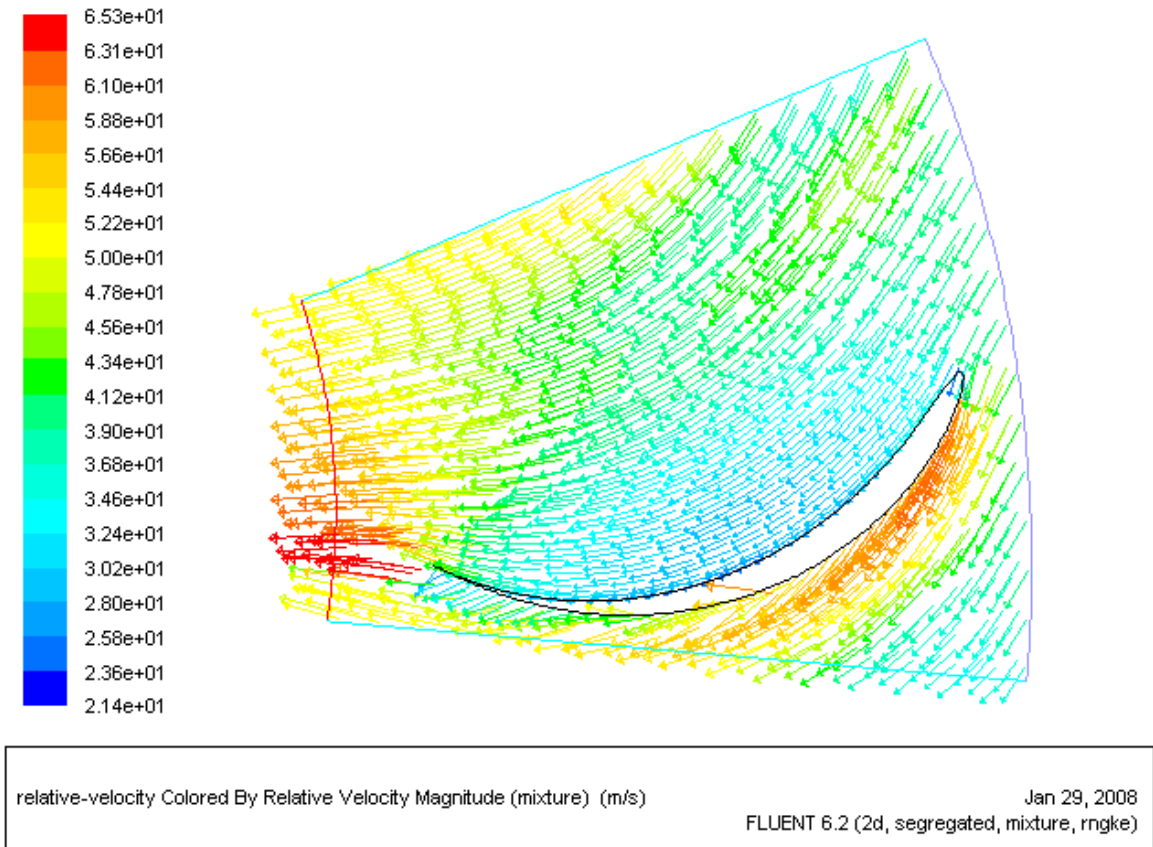


Figure 5.4 displays the relative velocity distribution along the blade profile. The relative velocity vectors indicate a smooth entrance of the flow. The flow direction on the pressure side follows the blade closely all the way to the exit. On the suction side, the vectors generally follow the blade contours except at the downstream section close to the walls where cavitation takes place and its displacement effect on the flow is felt. However, otherwise there was little difference in the flow pattern between the single and the two-phase flow predictions. Comparing between the relative velocity magnitudes on the pressure and the suction sides, it was found that they are higher on the suction side,

and this is to be expected since according to Bernoulli's Equation, the velocity magnitude is higher where the pressure is lower.

Figure 5.5 Contour Plot of the Volume Fraction of Liquid Water in the Mixture

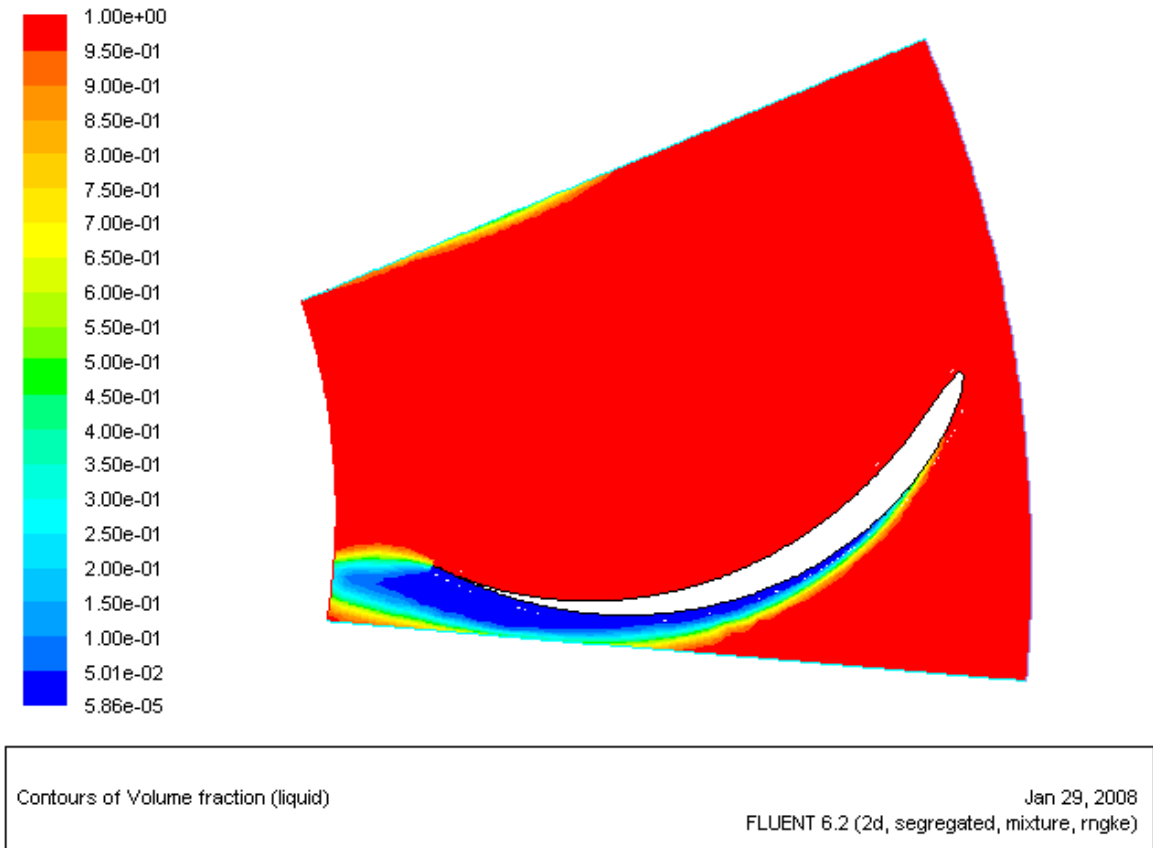
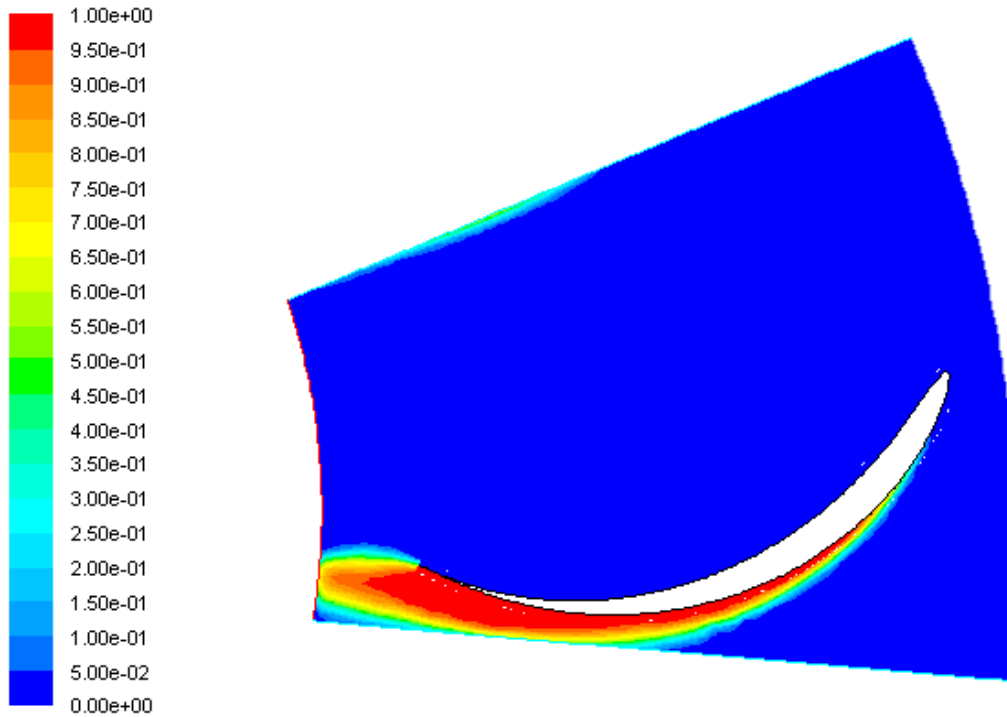


Figure 5.5 displays the volume fractions of the liquid water in the mixture for an inlet flow angle of 60 degree at a velocity of 40 m/s. The total volume fraction of the liquid water phase was 0.9868 (98.68 %), which indicates that most of the flowing field is filled with liquid. Vapor was observed only on the suction side of the blade and was more severe towards the trailing edge of the blade. That was where the cavitation occurs and it covers a fraction of about 0.013 (1.3 %) of the mixture in the flowing domain. This is to be expected since this region displays the lowest pressures.

Figure 5.6 Contour Plot of the Volume Fraction of Vapor in the Mixture



Contours of Volume fraction (vapor)

Feb 11, 2008
FLUENT 6.2 (2d, segregated, mixture, rngke)

Figure 5.6 displays the volume fraction of the vapor phase. It shows the exact inverse distribution to that of the liquid phase shown in Figure 5.5. This is to be expected since there are only two phases in one single material, thus the mixture fraction complements the other.

Table 16 shows the effect of cavitation on the prediction of discharge, torque, gross and net head, hydraulic losses and runner efficiency.

Table 16 Effect of Cavitation on the Flowing Properties

Flow Property	Without Considering Cavitation (Single Phase Modeling)	With the consideration of cavitation (Multiphase Modeling)
Discharge (m ³ /s)	29.1	29.1
Torque (MNm)	3.79	3.23
Gross Head (m)	311.4	286.6
Net Head (m)	226.0	233.8
Hydraulic Loss (m)	65.2	97.1
Runner Efficiency (%)	71.1	58.5

From the table above, it would be observed that cavitation has significant effect on the prediction of the torque, head, hydraulic losses and the runner efficiency. For a given flow rate, cavitation causes a reduction in the torque, the gross head and the runner efficiency prediction. It however, increases the predicted net head and hydraulic losses and this may explain why the unrealistic negative hydraulic losses were obtained with the single phase analysis; as well as the excessive runner efficiency that were observed with the single phase analysis for the case. Thus, despite the flow pattern remaining virtually the same for single and multiphase phase analysis, cavitation has a very significant effect on the performance predicted by the CFD analysis and should be considered in modeling a hydraulic turbine in which cavitation is likely to exist in order to accurately describe both the qualitative and quantitative features that occurs within the hydraulic turbine runner.

CHAPTER SIX

SUMMARY CONCLUSION, LIMITATION AND FUTURE EXTENSION

6.0 Summary Conclusion

The study focused on predicting the off design performance of an exceptionally low specific speed Francis' turbine. The specific speed was chosen to be exceptionally low in order to justify a two-dimensional investigation of the flow field. The blade to blade flow was studied in great detail for various flow inlet angles (guide vane angles) ranging from extreme off design up to and including design conditions. The flow was calculated employing a single phase model adopting the RNG turbulence model. The results were discussed and analyzed critically.

The analysis revealed unrealistically low negative pressures (pressures lower than absolute vacuum) were predicted. Apart from that, the flow field was plausible. A repetition of one of the cases employing a two-phase model with cavitation predicted results with realistic pressures. Thus it was concluded that to predict the flow field and performance characteristics of Francis' turbines correctly, one has to introduce two-phase cavitation models. Due to the difficulty of getting well converged solutions, and the large computational time and storage requirements of two-phase calculations, designers usually resort to only single phase calculations. However, the present research shows that this is not always acceptable.

6.1 Limitation of the Study

Due to time constraints, the study included only one two-phase flow calculation which corresponded to design conditions. Thus, the study did not examine the effect of cavitation prediction on all the characteristic curves obtained with the single phase analysis. The study was limited to two-dimensional analysis, and by necessity to a low speed Francis' turbine. The present study was also limited to constant flow rate conditions.

6.1 Future Extension

Further extension should be carried out to enable an in-depth cavitation analysis in order to determine the effect of cavitation on the various characteristic curves that were obtained with the single phase analysis. There will also be a need to determine which flow or turbulence properties that adversely affects the cavitation properties of the runner and how they can be altered to decrease (if not prevent) the occurrence of cavitation within the flow in a Francis' turbine. In that sense, further study needs to be undertaken to determine how other properties like the thickness and camber of the blade, and the degree of turbulence in the flow affects the pressure drop encountered within the flow at the suction side of the blade.

Future work may also be extended to study three-dimensional effects and to higher specific speed turbines depicting pronouncedly three-dimensional shapes. Further extension of the work could employ a constant gross head conditions rather than the constant flow rate employed in the present study. The effect of a draft tube may also be considered.

References

1. Shepherd D.G, (1956), "Principles of Turbomachinery", Macmillan Publishing Co., Inc, New York, U.S.A
2. Nilsson Hakan, (2002), "Numerical Investigation of Turbulent Flow in Water Turbine", Thesis for Degree of Doctor of Philosophy, Department of Thermo and Fluid Dynamics, Chalmers University of Technology, Goteborg, Sweden
3. Balje O. E., (1981), "Turbomachines: A Guide to Design, Selection and Theory", John Wiley & Sons Inc., New York, U.S.A
4. Sayers, A.T, (1990), "Hydraulic and Compressible Flow Turbomachines" McGraw-Hill Book Company, London, England
5. Kjolle Arne, (2001), "Hydropower in Norway", International Association of Hydraulic Engineering and Research Congress, Trondheim, Norway.
6. Nilsson H. and Davidson L, (August 2001), "A Validation of Parallel Multiblock CFD against the GAMM Francis' Water Turbine at the Best Efficiency and Off-Design Operating Conditions", Department of Thermo and Fluid Dynamics, Chalmers University of Technology, Goteborg, Sweden.

7. Drtina P., Keck H. and Sick M., (1997), “Breakthrough CFD Flow Simulation for a Complete Turbine”, Sulzer Management AG, Winterthur, Switzerland
8. Ruprecht A., Heitele M. , Helmrich T. , Moses W. , Aschenbrenner T., (2000), “Numerical Simulation of a Complete Francis Turbine including Unsteady Rotor/Stator Interactions”, Proceedings of the 20th IAHR Symposium on Hydraulic Machinery and Systems, University of Stuttgart, Germany .
9. Nennemann B., Vu T.C., Farhat M., (July 2005), “CFD prediction of unsteady wicket gate-runner interaction in Francis Turbine: A new Standard Hydraulic Design Procedure”, Waterpower V, Ausyyn, Tyyas, U.yyA
10. Guedes A., Kueny J., Ciocan GyD., Avellan F., (September 2002)yyyyUnsteady Rotor-Stator Analysis of a Hydraulic Pump-Turbine – CFD and Experimental Approach”, Proceedings of the XXIst IAHR Symposium on Hydraulic Machinery and Systems, Lausanne, Switzerland.
11. Ciocan G.D, Desvignes V, Combes J.F, Parkinson E., Kueny J.L , (1998), “Experimental and Numerical Unsteady Analysis of Rotor-Stator Interaction in a Pump-Turbine”, Proceedings of the 19th IAHR Symposium, September 1998, Singapore.
12. Versteeg H. K and Malalasekera W., (1995), “An Introduction to Computational Fluid Dynamics – The Finite Volume Method”, Longman Group Limited, England.

13. Bish Eric, (July 2001) "A Practical Tool", American Society of Mechanical Engineering Journal, Vol. 123/No. 7.

14. Organizing Committee of the 13th Annual Conference on Computational Fluid Dynamics, (July 31- August 3, 2005), "Proceedings of the Meeting to Discuss the Scope of the Conference", CFD Society in Canada, St. John, Canada.

15. Fluent News and Documentation, www.fluent.com, 2004-2005.

16. Susan-Resiga R, Ciocan G. D, (October 2004), "Swirling Flow Downstream a Francis Turbine Runner", Proceedings of the 6th International Conference on Hydraulic Machinery and Hydrodynamics, Timisoara, Romania.

17. Mauri S, Kueny J. L, Avellan F, (June 2000), "Numerical Prediction of the Flow in a Turbine Draft Tube Influence of the Boundary Conditions", Proceedings of ASME Fluids Engineering Division Summer Meeting, Boston, Massachusetts, U.S.A.

18. Susan-Resiga R, Avellan F, Ciocan G. D, Muntean S, Anton Loan, (June 2005), "Mathematical and Numerical Modeling of Swirling Flow in Francis Turbine Draft Tube Cone", Scientific Bulletin of the Politehnica University of Timisoara, Romania.

19. Burgreen G. W, Antaki J. F, Wu Z. J, Holmes A. J, (2001), “Computational Fluid Dynamics as a Development Tool for Rotary Blood Pumps”, McGowan Center for Artificial Organ Development, University of Pittsburgh, Pittsburgh, U.S.A.
20. Ruprecht A, (2000), “Unsteady Flow Analysis in Hydraulic Turbomachinery”, Institute of Fluid Mechanics and Hydraulic Machinery, University of Stuttgart, Germany.
21. Dai J, Ijichi N, Tange H, Shibata H, Tamaki H, Yamaguchi S, (2004), “Comparison of Internal Flow Filed Between Experiment and Computation in a Radial Turbine Impeller”, Japan Society of Mechanical Engineers International Journal, Japan.
22. Krivchenko G. I, (1986), “Hydraulic Machine-- Turbines and Pump”, MIR Publishers, Moscow
23. Stern F., Wilson R.V, Coleman H. W, Paterson E. G, (September 1999), “Verification and Validation of CFD Simulations”, Iowa Institute of Hydraulic Research Report No. 407, University of Iowa, U.S.A
24. Gorla Rama S.R, Khan Aijaz A., (2003),“ Turbomachinery – Design and Theory”, Marcel Dekker, Inc., New York.
25. User Guide, (1990-2000 Version.), DesignFOIL Demonstration Tutorial

26. Nilsson Håkan. and Davidson Lars, (2002), "A Numerical Investigation of Flow in the Wicket Gate and Runner of the Hölleforsen (Turbine 99) Kaplan Turbine Model", Department of Thermo and Fluid Dynamics, Chalmers University of Technology, Goteborg, Sweden
27. Nilsson Håkan. and Davidson Lars, (2002), "Validations and Investigations of the Computed Flow in the GAMM Francis Runner and the Hölleforsen Kaplan Turbine", Department of Thermo and Fluid Dynamics, Chalmers University of Technology, Goteborg, Sweden
28. Lecture Handout (2006), "Design of Francis' Turbine"

